EXPERIMENTAL INVESTIGATION ON THE CHARACTERISTICS OF THE ANNULAR TYPE COMPOSITE WICK HEAT PIPE

A Thesis

by

DAEGEUN KIM

Submitted to the Graduate and Professional School of
Texas A&M University
in partial fulfillment of the requirements for the degree of

MASTER OF SCIENCE

Chair of Committee,	Yassin A. Hassan
Committee Members,	Kalyan Annamalai
	Rodolfo Vaghetto
Head of Department,	Michael Nastasi

August 2022

Major Subject: Nuclear Engineering

ABSTRACT

An experimental investigation was conducted on the hydraulic characteristics of annular type wick structures for heat pipes. An experimental facility that can measure porosity, permeability and effective pore radius of the wick structures in a vacuum condition is established. Nine different multi-layered (6 layers in total) composite screen meshes are characterized. Based on the measurement results, a wick structure composed of one layer of 100×100 mesh, three layers of 400×400 mesh, and two layers of 60×60 mesh is determined to have the highest permeability to effective pore radius ratio (K/r_{eff}) and was selected as a targeted sample. The wick-to-wall gap effect on the hydraulic characteristics of annular type wick structure is also investigated by measuring the permeability and effective pore radius of the sample wick structure with varying gap widths. The result shows that the permeability increases as the gap increases from 0 mm to 1.2 mm. After a peak at 1.2 mm, the permeability decreases as the gap increases and converges to the value of the case measured without a wall structure. The effective pore radius becomes smaller as the gap increases, making a peak at a gap size of 1.2 mm. This result implies that there is an optimal point in gap size which is determined to be 1.2 mm for the selected composite mesh structure. To describe and model the advantage of this gap, the rising of a wetting liquid in the gap between a vertical solid plate and a mesh (with a small angle between them) was experimentally measured and analyzed. An additional experiment was performed to investigate the effect of curvature on the capillary rise using tubes and meshes of varying radii. Resultantly, we confirmed that the linear combination

of the contact angles of the solid plate and mesh could be applied to calculate the rising height from the Laplace–Young equation. Furthermore, the effect of curvature on the rising height of the liquid was negligible. We observed that a gap distance of 1.27 mm provided the largest permeability (K) over the effective pore radius (r_{eff}) value for a heat pipe with ethanol, which in turn resulted in the highest capillary limitation. Finally, an annular wick-type heat pipe is constructed and tested. The capillary limitation of the heat pipe showed good agreement with the suggested correlation. Additional research on measuring temperature distribution and visualizing the inside of the heat pipe is performed to understand the heat pipe behavior. A fiber optic sensor was used to measure the temperature distribution of the heat pipe during the transient and steady-state. Compared to the previously used sensors, thermocouples, for example, the fiber optic sensor provides more precise and detailed temperature data. A complete clear glass tube heat pipe was constructed using a transparent glass heater, allowing a fully visualized heat pipe experiment to observe the phenomena inside the heat pipe.

DEDICATION

I dedicate this thesis to my lovely wife, Jinhui, and my adorable daughter, Naeun. Without their support and encouragement, this work would not have been completed.

ACKNOWLEDGEMENTS

I would like to thank my committee chair, Dr. Yassin A. Hassan, for providing me with this great research and academic environment. I would also like to thank my committee members, Dr. Kalyan Annamalai, Dr. Rodolfo Vaghetto,

I would like to give special thanks to Dr. Joseph Seo who helped and guided the study of nuclear engineering. Also, I sincerely thank Dr. Se Ro Yang who gave me the opportunity to work on a great experiment with his valuable mentorship.

Finally, I really appreciate all my friends, colleagues, department faculties, and staff for allowing me to spend a great time at Texas A&M University

CONTRIBUTORS AND FUNDING SOURCES

Contributors

This work was supported by a thesis committee consisting of Professor Yassin A. Hassan, my advisor, and Professor Rodolfo Vaghetto of the Department of Nuclear Engineering, and Professor Kalyan Annamalai of the Department of Mechanical Engineering.

The experiments have been conducted with Dr. Joseph Seo and Hansol Kim who have studied together in the thermal-hydraulics laboratory advised by Dr. Hassan, and Dr. Vaghetto at Texas A&M University. The MATLAB codes utilized to analyze the experimental data were developed by Joeseph Seo. All other works conducted for the dissertation were completed by me independently.

Funding Sources

All my graduate study has been supported by a scholarship from the Republic of Korea Navy

NOMENCLATURE

ε	Porosity
r_{eff}	Effective pore radius
K	Permeability
m	Mass
ρ	Density
t	Time
Q	Heat pipe power
σ	Surface tension
g	Free-fall acceleration
μ	Dynamic viscosity
A	Cross-sectional area
H	Height
a	Angle (between two vertical plates)
x	Horizontal distance
αx	Gap distance at x position.
δ	Thickness
h_{lv}	Latent heat of the working fluid
L_{eff}	Effective length of a heat pipe
W	Watt
P	Pressure

G	Multiplying factor
R^2	Percentage of the response variable variation

TABLE OF CONTENTS

Page

LIST OF FIGURES

Page

LIST OF TABLES

Page

1. INTRODUCTION [*] [**]

A heat pipe is a passive heat transfer device having high thermal conductance and takes advantage of the thermal conduction of the solid enclosure and phase change of the interior working fluid (Peterson, 1994). The working fluid circulates passively inside the heat pipe due to the pressure gradient caused by phase change. This circulating working fluid intensively transfers heat from the evaporator region to the condenser region based on the principle of convection and phase change. Since their inception by Gaugler (Gaugler, 1944) and the independent invention by Grover (Grover et al., 1964), numerous efforts have been made to apply heat pipes to various industries on account of their high conductance and passive working characteristics. Initially, heat pipes were mostly applied to the cooling of spacecraft (Shukla, 2015). With the recent rise of the electronics industry, the application of small-sized heat pipes as cooling components in electronic devices having high heat-emitting density has been intensively studied (Khrustalev & Faghri, 1994). Furthermore, in the nuclear industry, heat pipes were proposed as a passive cooling system of nuclear power plants in a station black out (SBO) scenario due to beyond design-basis accidents (BDBA) (Jeong et al., 2015; Mochizuki et al., 2014). Subsequently, several

---

studies were conducted to utilize the heat transfer characteristics of heat pipes more actively for power generation and storage systems rather than for cooling applications. For example, a heat pipe system for increasing the efficiency of solar cells has been actively discussed in the research of renewable energy (Mathioulakis & Belessiotis, 2002). In addition, several studies are being conducted to apply liquid metal heat pipes as the primary heat transfer system in micro nuclear reactor (Yan et al., 2020). The utilization of heat pipes for micro reactors allows for a compact design with a high power density. Moreover, the nature of heat pipes enables their application in reactors. Consequently, researchers have proposed and studied heat pipes with varying working fluids and operating temperatures. The Kilopower and SAIRS micro reactors use heat pipes with sodium (Na) as the working fluid and their target operating temperature is 1050–1200 K (El-Genk, 2004; Mohamed S. El-Genk and Jean-Michel P.Tournier, 2004; Palac et al., 2016). Heat pipes with sodium and potassium (Na/K) as their working fluid are used for HOMER15/25 and eVinci having a target temperature range of 880 K-920 K (Levinsky et al., 2018; Poston, 2000). The heat pipes in MSR-A and HP-STMCs use lithium (Li) as the working fluid and operate between 1500 and 1800 K (Bushman et al., 2004; El-Genk, 2004), whereas the MSR-B uses K as the working fluid and operates between 930 and 1500 K (Mcclure et al., 2015). Notably, most of the heat pipes considered for utilization in micro reactors have an annular-type wick structure.

The classification of heat pipes can be achieved by considering the source of force used to return the condensed fluid from the condenser region to the evaporator region. For example, a wickless heat pipe, also called a thermosyphon, uses gravity to transfer liquid

to the evaporator. A heat pipe with wick, which is the most common type, uses capillary force generated by porous media as the source of liquid transport. This type of heat pipe can be used irrespective of the direction of heat transfer to gravity, which is a huge advantage in its range of applications. In this study, particularly, an annular wick-type heat pipe is investigated. Since the primary heat transport medium is liquid, characteristics of the wick structure dominate the overall performance of the heat pipe. An annular porous wick structure is demonstrated in Sockeye which is a heat pipe analysis application based on the Multiphysics Object-Oriented Simulation Environment (MOOSE) finite element framework (Hansel et al., 2021). The main purpose of Sockeye is to provide a transient heat pipe simulation tool to be used in the analysis of nuclear microreactor designs. Therefore, the study of the properties of the annular shape wick used in Sokeye can provide useful data for future research on nuclear micro reactors. Since the primary heat transport medium is liquid, characteristics of the wick structure dominate the overall performance of the heat pipe.

A heat pipe with an annular-type wick structure is characterized by the exitance of a gap between the wick structure and tube wall. The flow characteristics of a fluid inside a porous media must be considered to determine the benefits of this type of heat pipe for the heat transfer in a micro reactor. Based on the fluid dynamics of porous media, the wick structure can be characterized by several parameters, such as porosity (ε), effective pore radius (r_{eff}), and permeability (K) (Manoj et al., 2013). The porosity of a porous medium is defined as the volume ratio of voids inside it relative to its total volume. Pore radius, or pore size, is the average size of voids inside the porous material. It is directly related to

the capillary pressure, according to the Laplace–Young equation. This value must be sufficiently small to generate a large capillary pressure difference between the evaporator and condenser areas. Furthermore, permeability refers to the resistance of the wick structure against the fluid flowing inside it. This value must be sufficiently large to generate a low liquid pressure drop across the wick structure (Faghri, 1995) during its travels in the axial direction. In addition to these hydraulic parameters, the thermal conductivity, or effective thermal conductivity, is related to the thermal characteristics of the wick structure. However, the thermal conductivity is not handled in this study as we focused only on the capillary limitation of the heat pipe.

According to the aforementioned description, wick structures having a small pore radius and high permeability are recommended for increasing capillary pressure and reducing the pressure drop of the liquid flow in heat pipes. However, the combination of a small pore radius and high permeability is difficult to accomplish in the majority of homogeneous wick designs that have pores of uniform size (Faghri, 1995). In other words, the two parameters become competing factors to each other in a homogeneous wick. A homogeneous wick with a small pore radius might have high capillary pressure but it also has a small permeability which will create high resistance to the liquid flow. There can be two ways to overcome this problem. First, a heterogeneous wick structure, or composite wick structure, which consists of distributed pore sizes, can be used. The wick combining coarse and fine wick has superior performance since heat pipe performance requires high capillary pressure, and yet still offers low resistance to fluid flow (Mwaba et al., 2006). The composite wick structures provide high capillary pressure by having small pores while

employing high permeability from large pores. The simplest composite wick can be constructed by wrapping multiple layers of screen mesh with different pore sizes, which is a multi-layered composite mesh screen wick (Faghri, 1995). The other way to overcome the tradeoff problem of the pore size and the permeability is to introduce an extra flow path for liquids other than wick structures. A heat pipe with an annular type wick structure, for example, has a gap space between the tube and the wick structure. Since condensed fluid can travel through the gap, the heat pipe with an annular wick has a significantly lower pressure drop when it is compared to the heat pipe with a homogeneous wick (Pauluis & Lang, 1976). The advantage of introducing the gap can be more clearly emphasized when the pressure drop values for the gap and porous media are quantitively compared. Assuming a laminar flow over 1m of the channel, water experiences approximately 6 times smaller pressure drop when it travels through the 0.7 mm gap instead of a porous media with 10^{-11} m^2 of permeability from the calculation using Darcy's law. In this study, an annular heat pipe with a composite wick and gap has the shape shown in Figure 1.

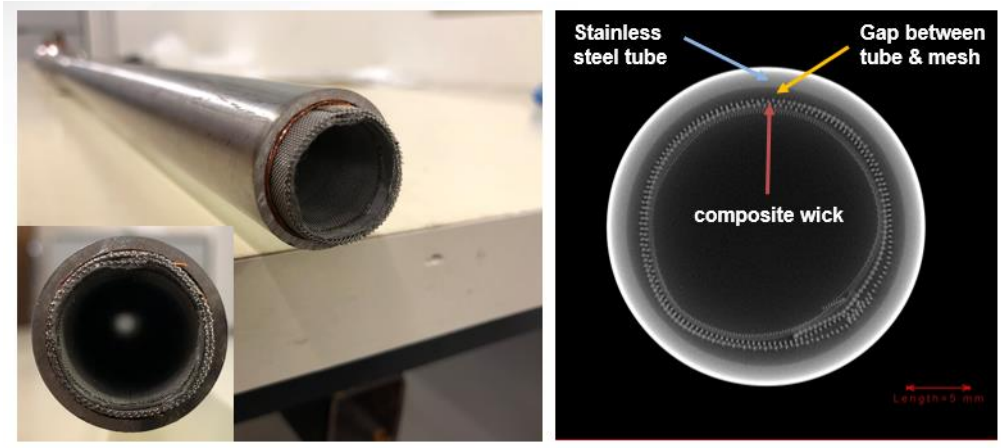

Figure 1. Sample structure of annular heat pipe with composite wick and gap

Recently, the implementation of the annular composite wick heat pipe as a principal heat transmission system of the micro reactor is being carefully examined due to its merits indicated above. Failure of a heat pipe can result in serious contamination issues, such as the leakage of working fluid. Also, the user cannot adjust the operating characteristics of the heat pipe after installation because it is a passive device. As a result, for the reactor's safety and durability, the performance of the heat pipe under various conditions should be investigated. Pauluis and Lang used a theoretical approach to analyze the pressure drop in the wick structure of annular wick heat pipes using hydrogen, nitrogen, and oxygen as working fluids (Pauluis & Lang, 1976). The steady-state cyclic performance of a sodium heat pipe reactor was investigated by Paripatyadar and Richardson using a daily solar cycle in the 600–900 C range (Paripatyadar & Richardson, 1988). Richardson et al. simulated and tested a sodium heat pipe reactor, obtaining data such as axial and radial temperature profiles, energy flux transformation, and flux profiles for each temperature range (Richardson et al., 1988). Rosenfeld et al. reported on the operating lifetime and reliability of sodium heat pipes with different wall materials (Rosenfeld, 2004). Gotoh and Hill investigated the stability and reproducibility of sodium heat pipes (Gotoh & Hill, 1992). Reid et al. measured the heat rejection rate in the operating temperature range of 13 sodium heat pipes using the SAFE-30 core configuration (Reid, 2003).

Despite previous efforts made on the characteristics of annular wick type heat pipe, the number of studies related to the heat pipe design and modeling is still very limited due to the hardness of experiments. To the author's best knowledge, there is a huge lack of

experimental data and models that can support the design of the annular type composite wick heat pipe. To be specific, important design parameters that might seriously affect the performance of the heat pipe such as the composition of the wick structure and gap distance have not yet been studied even though the importance of these parameters becomes more apparent. The importance of the research increases when the predictions of the heat transfer performance and the operating limitations are directly related to the safety of the system. In the application of the heat pipe into a high temperature micro nuclear reactor, for instance, an experimental investigation of the design parameters and models is necessary to determine heat pipe performance in continuous operation as well as the safety margins of the system, which is the primary motivation of this study.

Additionally, it is interesting to observe how the composite wick and gap of the heat pipe mentioned above change the fluid flow properties inside the pipe, but relevant researches are insufficient. This fluid flow feature has a substantial effect on the temperature gradient of the entire heat pipe system and consequently affects the heat pipe’s conductivity, which is an indicator of the heat pipe's performance. For example, while numerous investigations have been performed recently on the effect of a heat pipe's Geyser boiling phenomena on its stable operation, there are relatively limited observational studies on the internal phenomenon. As a result, observing the temperature change inside the heat pipe using high-tech temperature measuring sensors such as fiber optic sensors in the experimental heat pipe is informative. Furthermore, fabricating a transparent heat pipe and visualizing what is happening in the heat pipe also could provide highly valuable research data.

In this study, therefore, the characteristics of the annular type composite wick structure are intensively studied. A total of nine combinations of the multi-layered screen meshes are constructed and their performances are tested. Also, the effect of the wall on the performance of the wick structures with different gap sizes is noted. The performance of wick structures is characterized using K/r_{eff} values. And then it was extended by developing a methodology to find an optimal gap distance for the capillary limitation of heat pipes that can be used for a wide range of geometry and working fluids. The method previously introduced requires time evolution of rising height information of liquid in a gap between mesh structure and the wall surface to obtain K/r_{eff} value. In this study, the time series of the liquid mass at varying gap distances is analytically calculated by referring to the previous study performed by Higuera et al. (Higuera et al., 2008). A non-dimensional solution of the capillary rise between two solid plates making a small angle between them was suggested in the referred study. We try to utilize the solution to analyze capillary pressure caused by the gap in the annular wick-type heat pipe. To perform the analysis, the applicability of the solution from Higuera et al. (Higuera et al., 2008) to this study should be tested, focusing on two differences. First, the gap in the annular wick-type heat pipe is composed of a solid surface and mesh surface, while the non-dimensional solution is given for two solid surfaces. Second, the gap in the heat pipe has a curved surface, while Higuera et al. suggested their solution for flat, straight plates. Therefore, in this study, the capillary rise in the gap between two different materials will be investigated using simple experiments based on the study by Bullard and Garboczi (Bullard & Garboczi, 2009). Furthermore, additional experiments will be conducted to determine the

effect of curvature on the capillary rise in the annular wick-type heat pipe. After confirming the applicability of small experiments, the study by Higuera et al.(Higuera et al., 2008) will be extended to obtain the time evolution of the rising height of any type of Newtonian fluid by leveraging the advantage of a non-dimensional (or normalized) solution.

Figure 2. Transparent Glass Heater

The results obtained from the wick characterization experiment are expanded to the heat pipe performance experiment. The capillary limitation of the heat pipe is determined, and some model that can include an understanding of the wick characterization is suggested. The work will increase insight into understanding heat pipes with annular type composite wick structures. Also, the data and model provided in this study might help to build a heat pipe with optimized performance in a targeted condition. Furthermore, In the heat pipe performance experiment, an optical fiber sensor is installed inside/outside the heat pipe to accurately observe the temperature distribution at each position and the temperature change trend of the heat pipe could be visually observed. Finally, the heat pipe's performance experiment is converted into a visualization

experiment. The stainless steel tube of the heat pipe is replaced with a transparent glass tube. The evaporator which was wrapped by the heater is changed to a clear glass heater as shown in Figure 2. The entire heat pipe is made transparent, allowing for visualization of the heat pipe's interior phenomena. By making the entire heat pipe transparent, the internal phenomenon such as boiling patterns of working fluid is visually observed. Information visually observed through high-speed cameras and infrared cameras is recorded as data and analyzed. The work will increase insight into understanding heat pipes with annular-type composite wick structures. Also, the data and model provided in this study might help to build a heat pipe with optimized performance in a targeted condition.

2. EXPERIMENTAL METHOD[*] [**]

The experimental component of this study is divided into four components. The first study examines the characteristics of the composite wick structures with varying wick compositions. Measurements for porosity were made, followed by an experimental procedure to determine the permeability and effective pore radius. This ratio, K/r_{eff} is an important indicator for heat pipe performance. The effect on K/r_{eff} due to the gap size between the wick structure and the wall is also investigated. As mentioned in the previous section, the resistance of the flow for the annular wick type heat pipe appears as a combination of Darcy flow in the porous media and laminar flow in the annulus. In this case, K/r_{eff} of wick and wall assembly can usefully explain the combined resistance and is used as an indicator of the heat pipe performance in terms of capillary limitation.

In the second study, the hydraulic properties of the gap for the annular wick type heat pipe have been experimentally investigated. when the distance between two flat plates is sufficiently narrow, capillary force is generated. Although mesh is a porous medium rather than a solid surface, it still generates capillary force. Three cases are examined to determine the capillary force of the gap: two solid plates, a solid to mesh plate, and two

---

[*] Reprinted with permission from "An experimental investigation on the characteristics of heat pipes with annular type composite wick structure" by Joseph Seo, Daegeun Kim, Hansol Kim, and Yassin Hassan, 2022, Nuclear Engineering and Design, vol. 390, 111701, copyright 2022 by Elsevier B.V. All rights reserved.

[**] Reprinted with permission from "Design Optimization of Gap Distance for the Capillary Limitation of a Heat Pipe with Annular-Type Wick Structure" by Joseph Seo, Daegeun Kim, Hansol Kim, and Yassin Hassan, 2022, Physics of Fluids, vol. 34, 067116, copyright 2022 Author(s). Published under an exclusive license by AIP Publishing.

mesh plates. The method of observing a capillary rise is used in this study to estimate the contact angle of the mesh screen wick material. While solid materials have known contact angles, porous media such as mesh wicks have no contact angle data, so they should be measured by the experimental method. The work will increase insight into understanding annular wick type heat pipes with a gap.

Results obtained from the wick characterization experiment are then expanded to a heat pipe performance experiment, which is the third study. A heat pipe is constructed with the mesh composition determined to have the highest K/r_{eff} value. After operating this heat pipe at a range of temperatures and power levels, the capillary limitation of the heat pipe is determined, and a model reflecting the wick characterization is presented. This work will provide valuable insights into heat pipes with annular type composite wick structures. The data and model produced by this study will help to design heat pipes with optimized performance under required conditions. In addition, while experimenting, a fiber optic sensor is used to determine the overall temperature distribution and internal temperature change of the heat pipe.

Finally, a transparent heat pipe is constructed for the heat pipe visualization experiment, and the flow characteristics within the heat pipe are visually observed and recorded. These studies will shed light on heat pipes with annular composite wick structures. These research data and models will contribute to the construction of heat pipes with optimized performance.

2.1. Wick Characterization Experiments

2.1.1. Wick Structure Construction

In this experiment, 9 wick variations, each with 6 mesh screen layers, were constructed using three types of mesh: 60 by 60, 100 by 100, and 400 by 400. Detailed information on the 9 samples is shown in Table 1. Because wick structures are constructed manually in this study, there will be uncertainties caused by the manufacturing process. The uncertainties are quantified by replicating the construction of each of the 9 cases 12 times. The porosity of 12 meshes is measured by the method introduced in the next section, and the deviation of the measurement is determined to quantify the uncertainty. The results showed that the measured porosities of 12 meshes have a standard deviation of ±0.81% in comparison with the average value.

Table 1. Composition of the multi-layered composite screen wicks

Case #	Total number of layers	Mesh composition		
		100-mesh (inside layer)	400-mesh (middle layer)	60-mesh (outside layer)
1	6	6	0	0
2		0	6	0
3		0	0	6
4		2	2	2
5		1	3	2
6		2	3	1
7		2	1	3
8		3	2	1
9		3	3	2

To build the wick sample, each mesh screen was cut to be 25.4 mm by 101.6 mm. Six mesh screens were stacked on top of each other in the order shown in Table 1. The edges of the stacked meshes were then spot-welded to create a bond between adjacent meshes. The constructed mesh structures were thoroughly washed using 70 % isopropyl alcohol as a final step. Figure 3 shows the configuration of the wick assembly for the wall

effect experiment. It is composed of a wall with a clamp at the top, the wick, and the shim structures. Shim structures were inserted between the wall and the wick in the clamped section of the assembly to create a controlled gap size ranging from 0 mm to 20 mm.

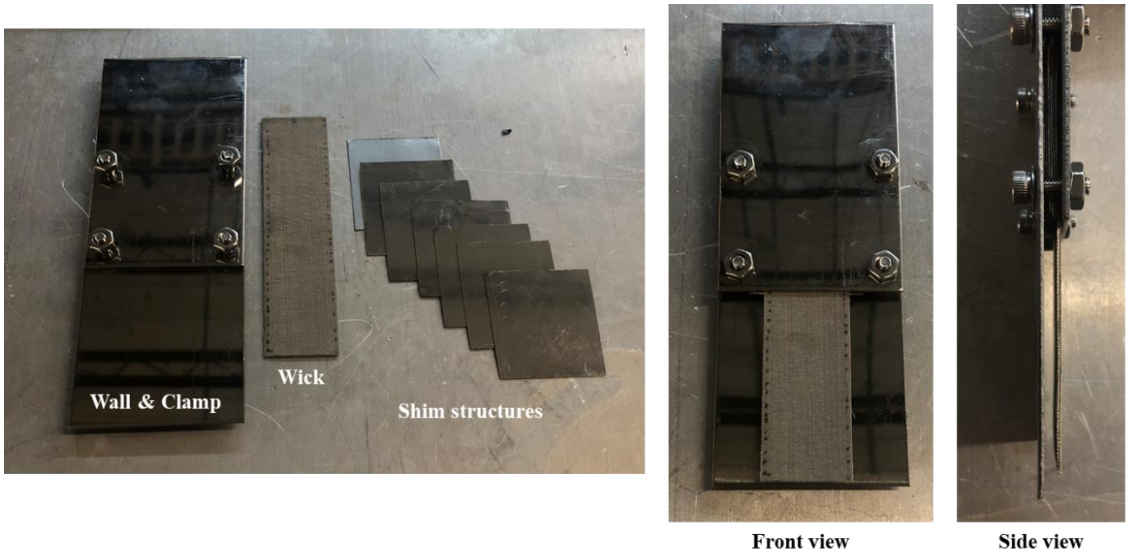

Figure 3. The configuration of the wick assembly for the wall effect experiment.

2.1.2. Porosity Measurement

Porosity is a ratio of the void volume in a porous media over the total volume. In this study, mass and density data are used to measure the porosities of different wick structures. Considering the time required for wetting and drying, ethanol is used as a wetting fluid. A bench-top digital scale with ±0.001 g of resolution (or readability) is prepared to measure the mass of the dry and wet mesh. The void volume of a mesh can be obtained from the ethanol mass required to fully wet (or saturate) the mesh. As shown in Figure 4, first, the mass of dried mesh (m_{mesh}) is measured using the scale. Then, the mesh was fully immersed in ethanol for about 10 seconds before being weighed again. By subtracting the mass of dried mesh from the saturated mesh, the amount of liquid inside

the mesh (m_{liquid}) is determined. The porosity is calculated using the known density of the ethanol and mesh using Eq. 1

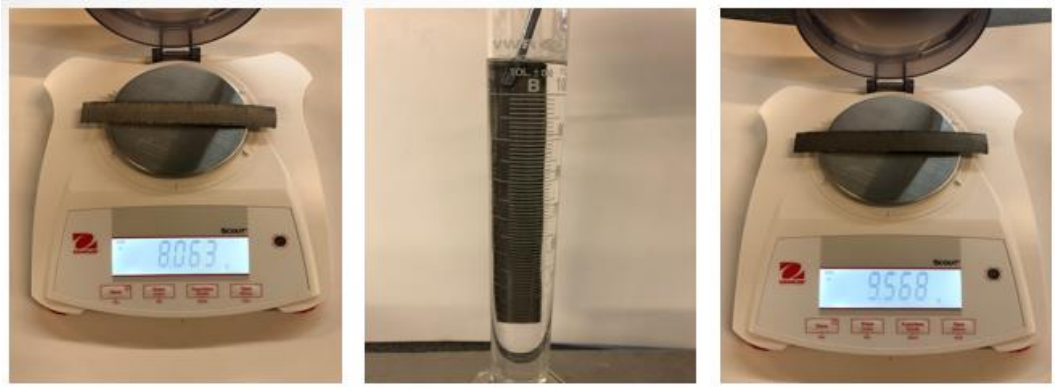

Figure 4. Porosity Measurement Procedure

$$\frac{1}{\varepsilon} = 1 + \frac{m_{mesh}\rho_{liquid}}{m_{liquid}\rho_{mesh}} \qquad \textbf{Eq. 1}$$

Uncertainty is introduced into this procedure by both the scale and liquid loss due to evaporation, a difficult value to quantify. Thus, the same procedure is repeated 10 times to obtain the averaged mass data. The result showed a standard deviation of $\pm$0.30%.

2.1.3. Permeability and Effective Pore Radius Measurement

To measure permeability and effective pore radius of each wick sample, the method suggested by Holley and Faghri (Holley & Faghri, 2006) was used. In this method, a transcendental equation based on mesh geometry, fluid properties, and the height of a rising liquid at a given time is derived using the pressure balance for the rise of liquid in a vertical wick. Because the exact location of a liquid front can be difficult to determine in the case of a non-homogeneous wick structure, the height is substituted with the mass of the rising liquid. This produces the following equation:

$$t_{Holley\&Faghri} = f(K, r_{eff}, m_{\exp}) = -\frac{\varepsilon \mu_l}{\rho_l^2 g^2 K}\left[\frac{2\sigma}{r_{eff}}\ln\left(1-\frac{g r_{eff}}{2\sigma A_{wick}\varepsilon}m_{\exp}\right)+\frac{g}{A_{wick}\varepsilon}m_{\exp}\right] \quad \textbf{Eq. 2}$$

Here, g is gravitational acceleration, ρ_l is the density of the working fluid, σ is the surface tension of the working fluid, A_{wick} is the cross-sectional area of the wick, μ_l represents the viscosity of the working fluid. When the liquid properties and geometric parameters are known, the time variable, $t_{Holley\&Faghri}$, can be calculated from three unknown values, permeability (K), effective pore radius (r_{eff}), and mass of the liquid (m_{exp}) pulled up by the mesh. By introducing a variable for experiment time (t_{exp}), as shown in Eq. 3, and performing a vertical liquid rising experiment using a sintered mesh sample, Holley and Faghri obtained several pairs of mass (m_{exp}) and time (t_{exp}) data. Then, to find the solution, a sample space of permeability and effective pore radius was set, and the result of the mean absolute percent deviation of time values (t_{exp}) of the data set from calculated time ($t_{Holley\&Faghri}$) was plotted in space. The true values for permeability and effective pore radius were then determined to be where the error between t_{exp} and $t_{Holley\&Faghri}$ was smallest.

$$t_{\exp} - t_{Holley\&Faghri} = f(K, r_{eff}, m_{\exp}, t_{\exp}) = t_{\exp} + \frac{\varepsilon \mu_l}{\rho_l^2 g^2 K}\left[\frac{2\sigma}{r_{eff}}\ln\left(1-\frac{g r_{eff}}{2\sigma A_{wick}\varepsilon}m_{\exp}\right)+\frac{g}{A_{wick}\varepsilon}m_{\exp}\right] = 0$$

$$\begin{cases} t_{\exp} = (t_1, t_2, t_3, \cdots, t_n), \\ m_{\exp} = \left(m_{t=t_1}, m_{t=t_2}, m_{t=t_3}, \cdots, m_{t=t_n}\right) \end{cases} \quad \textbf{Eq. 3}$$

The approach introduced above is adopted in this study. Figure 5 shows the experimental setup for measuring the permeability and effective pore radius of the wick structures. An acrylic vacuum chamber was prepared and connected to a vacuum pump to

obtain a vacuum condition inside. A vacuum pump with 1.5×10^{-2} torr of maximum vacuum pressure and 4.72 liters per second (LPS) of max flow rate was used in this study. The vacuum pressure was monitored by an analog pressure gauge connected between the vacuum chamber and the pump. A rod of 3.18 mm in diameter was installed through the top of the chamber using an O-ring compression fitting. The fitting allows the rod to move up and down while maintaining the vacuum condition in the chamber. The dried wick structure (or the wall and mesh assembly in the case of the wall effect experiment) was placed in the chamber held by a clamp at the end of the rod. A bench-top digital scale with ±0.001 g of resolution (or readability) was located at the bottom of the vacuum chamber. The repeatability (or standard deviation) of the scale was ±0.002 g. A petri dish filled with 99.9% pure ethanol was placed on the scale and used to measure the rising speed of the fluid.

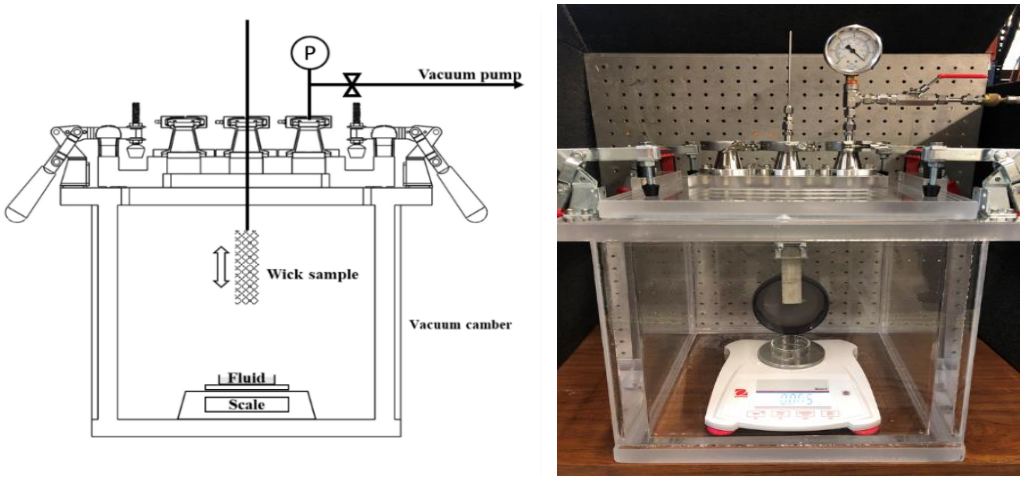

Figure 5. The schematic (left) and picture (right) of the wick characterization experimental setup

The experiment begins by filling the petri dish with ethanol up to a specified level and taring the scale. The wick is fixed and the vacuum flange (top cover of the vacuum

chamber) is attached to the chamber. The chamber is vacuumed down to -90 kPa of vacuum pressure using the vacuum pump. Then, the wick is slowly lowed toward the petri dish. When the wick reaches the fluid and its tip is submerged into ethanol, the wick is stopped and its height is maintained. The reading of the scale is recorded using a camera with 30 fps of capturing frequency. After the wick is determined to be saturated by checking the change of mass, the valve of the chamber is opened to recover the pressure, and the wick is removed from the chamber.

In Figure 6, the mass retained by the composite mesh case number 8 in Table 1 is shown as an example. It can be noticed that the rate of mass decreases during the measured time and becomes saturated after several minutes. From the data, five pairs of time and mass are selected. In this study, 0.667, 1.67, 3.33, 5.00, and 6.67 s of time and the mass at those time values are used to calculate the permeability and effective pore radius of the wicks.

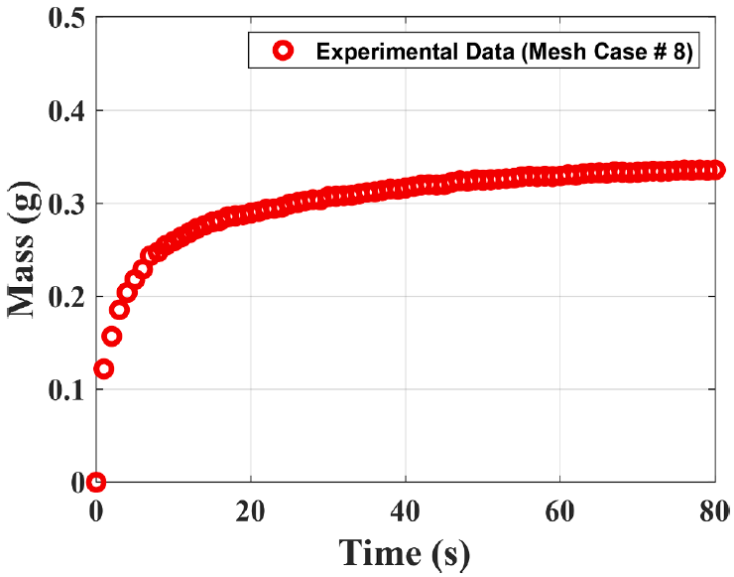

Figure 6. The example of the mass retained by the composite mesh (Case #8)

2.2. Capillary Rise and Contact Angle Experiment

2.2.1. Capillary Rise of Liquid in Gap between Two Plates

Surface tension is often explained using the phenomenon of capillary rise in thin tubes. However, in this case, we used the example of capillary rise between two small plates creating a thin wedge (Piva, 2009) to demonstrate capillary rise between the solid surface and the screen mesh. As surface tension supports the weight of the elevated liquid, we used Eq. 4 to obtain the height of capillary rise of the liquid, H, as follows:

$$H = \frac{2\sigma\, cos\theta}{\rho g(ax)} \qquad \textbf{Eq. 4}$$

Where θ is the contact angle between the liquid surface and the wall, g is the free-fall acceleration, ρ is the liquid density, x is the horizontal distance measured from the point where the two plates meet and αx is the gap distance at x position. Figure 7 shows the schematic sketch.

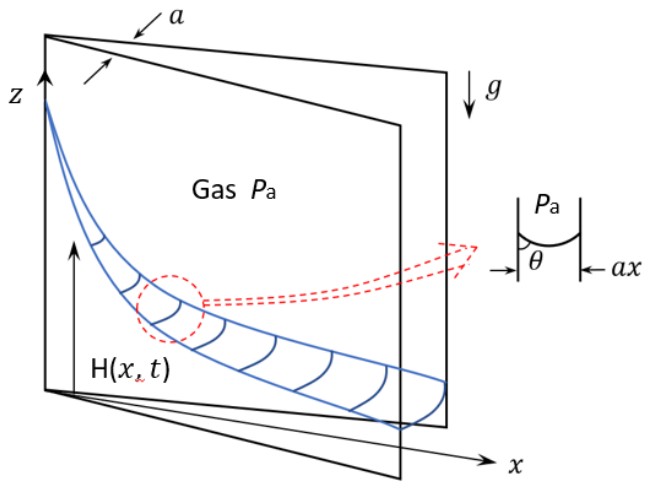

Figure 7. Schematic sketch of capillary rise between the plates with a small gap.

However, Eq. 4 does not accurately describe the capillary rise between solid and screen mesh surfaces due to the different contact angles on each side. Hence, we used Eq. 5, which explains the capillary rise between different materials (Bullard & Garboczi, 2009). Generally, when two walls have dissimilar geometries, the contact angle θ_0 at one of the walls is different from the contact angle θ_1 at the other wall. In this study, for the case of the gap in an annular heat pipe, the outer wall was made of glass and the inner wall was the steel mesh.

$$H = \frac{\sigma\,(cos\theta_0 + cos\theta_1)}{\rho g(ax)} \qquad \textbf{Eq. 5}$$

In this experiment, stainless steel mesh (100 by 100) and glass plates are prepared to make a gap. The experimental setup of the angled mesh-plate experiment is shown in Figure 8. The main purpose of this experiment was to check the applicability of Eq. 5 in the combination of mesh and solid surface. Square plates made of glass and a mesh screen of the same size (15×15 $cm^{2)}$ were prepared. Three samples (glass × glass, glass × mesh, mesh × mesh) were constructed with one side stayed contact with the other along a vertical edge. Spacers having a thickness of 4.75 mm were placed at the other end, to set an angle of 3.17° between the plates. Thereafter, the samples were placed inside a vacuum chamber. After their lower edges were introduced into ethanol, vacuum pressure (-90 kPa, 0.1 bar) was achieved using a vacuum pump. The liquid level was initially captured using a camera, and the curve of the rising height was obtained using image processing.

Figure 8. Experimental setup of the angled mesh-plate experiment (Glass-Glass / Glass-Mesh)

2.2.2. Contact Angle Measurement of Wick Structure

The above experiment may be used to determine how much ethanol liquid rises in relation to the distance of the gap in the form of a graph. The validation of the rising height experiment can be simply performed by comparing it with the calculation result of Eq. 5. To do so, contact angle measurement is required. There are several methods for measuring the contact angle of a liquid with a solid surface, such as confocal microscopy techniques (Sundberg et al., 2007), the Wilhelmy method (Wilhelmy, 1863), atomic force microscopy (AFM) (Nguyen et al., 2003; Pompe & Herminghaus, 2000), and the droplet image analysis method, which is the most commonly used method during these years (Schuster et al., 2015; Zhao & Jiang, 2018). However, these common measurement techniques are unsuitable for mesh due to liquid imbibition into the media. Thus, a direct observation approach was used in this study to determine the contact angle. The screen mesh was immersed vertically in ethanol. A vacuum environment was established for the measurement, and the angle formed by the ethanol was measured after a long period (~ 24 hrs) to attain the steady-state. The contact angle of the borosilicate glass was measured

with the same procedure but with a smaller period (~ 10 mins) to obtain a steady-state. The camera with 200mm of focal length was set at the position with 1 m of distance. The inclination angle and position of the camera are precisely adjusted to make its viewing plane perpendicular to the liquid surface. After capturing the image of the contact angle, the structures were removed from the vacuum chamber and dried. The overall procedure was repeated ten times to check the repeatability and uncertainty. The standard deviation of the contact angles from repeated measurements is considered an error of the measurement. As shown in Figure 9, the contact angle of ethanol on glass and mesh were 36° ± 0.59° and 58.4° ± 2.57°, respectively. This data was employed as contact angle information for the surface of the screen mesh.

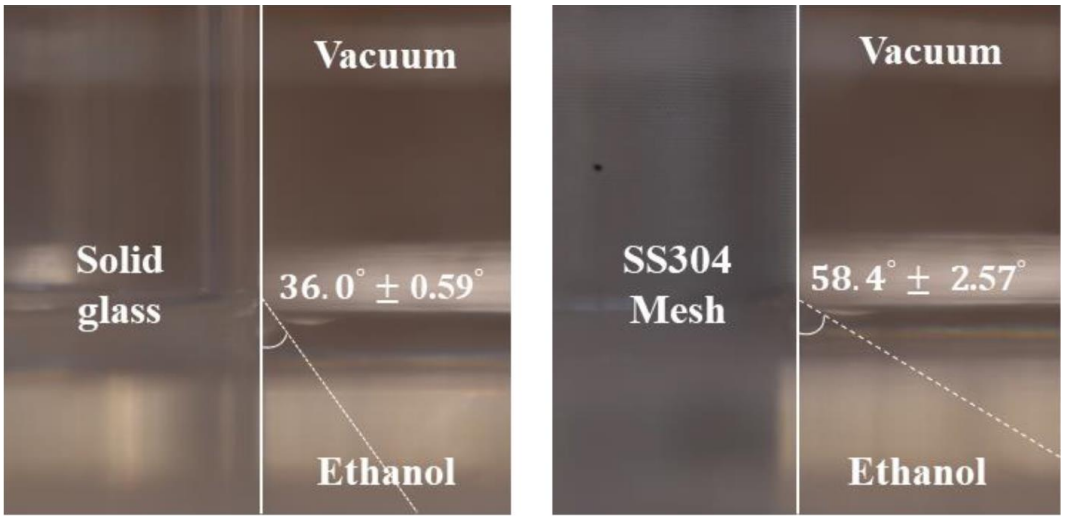

Figure 9. The result of contact angle measurements of glass-ethanol (left) and stainless steel mesh (100 mesh)-ethanol (right).

2.2.3. Curvature Effect of the Capillary Rise

The inner wick structure of the annular heat pipe was curved and not planar. The applicability of the results from flat plates to such curved geometry may be questionable.

Considering that the distance term of the Laplace-Young equation stands for both the diameter of a circular tube and the gap between two flat plates, we inferred that the effect of curvature on the capillary rise is negligible. However, this has not yet been experimentally proved for the present case where one side of the gap is a porous medium. Thus, comparing the capillary rise between flat plates and between curved surfaces is essential. The capillary rise between the curved mesh and glass surface was investigated and compared to the capillary rise between the flat plates to determine the rate of discrepancy due to the curvature of the geometry. Figure 10 illustrates the curvature experimental setup.

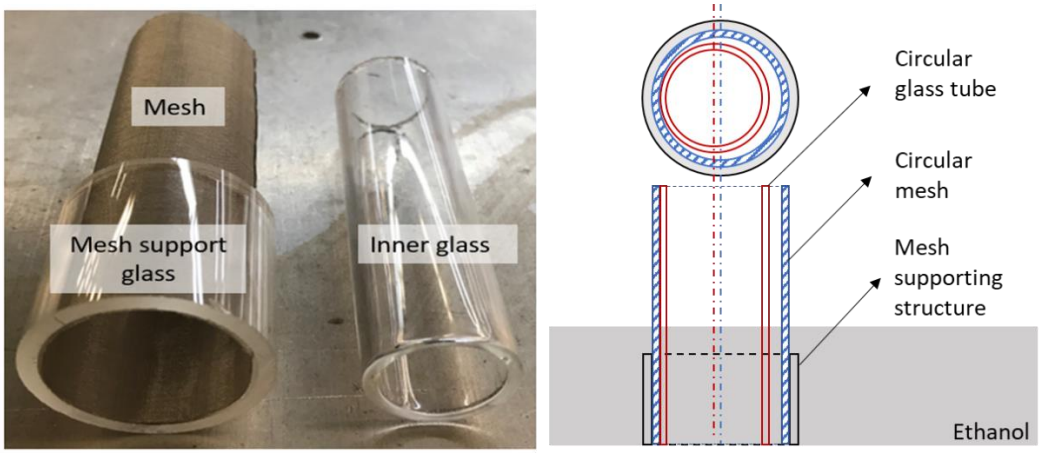

Figure 10. Tubes and mesh structure (left) and the schematic of curvature experimental setup

The experimental setup consisted of three parts: a cylindrical mesh structure (100×100 mesh), a mesh support glass, and an inner glass. The cylindrical mesh structure was fabricated by wrapping the mesh around a steel rod of the desired size and spot welding the edges to maintain the cylindrical shape. Due to the flexibility of the mesh surface, the support glass was introduced as a holder to support the mesh structure in

maintaining its perfect cylindrical shape. To avoid distortions induced by glass refraction while observing the capillary rise, a glass tube was placed inside the mesh structure to act as the inner surface of the narrow gap. The inner diameter of the mesh structure was 31.4 mm, and the outer diameter of the glass tube was 25.4 mm, which resulted in a maximum gap distance of 6 mm.

An angle reference line was necessary for comparing the capillary rise observed on a curved surface with that observed on a flat surface. Figure 11 shows the angle reference lines. Because capillary rise is affected by both the inner and outer surfaces, the angle reference line must be based on the angle of the middle circle; thus, the gap was constantly increased from 0 to 6 mm with the angle.

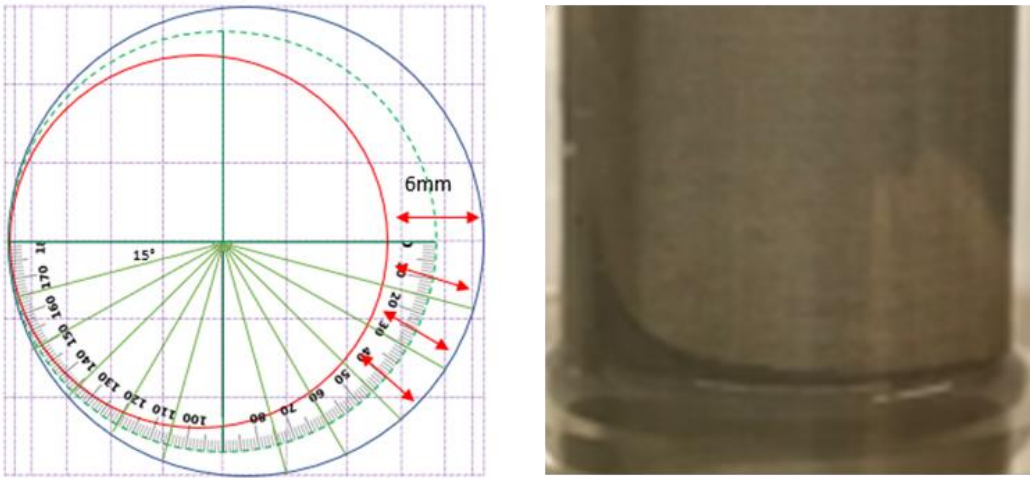

Figure 11. Angle reference lines for flattening (left) and an example of rising height image (right)

2.3. Heat Pipe Performance Experiment

2.3.1. Heat Pipe Construction

In this study, an annular type multi-layered rolled composite screen mesh made of stainless steel is used as a wick structure of the heat pipe. The cross-sectional imaging of

the heat pipe, shown in Figure 12, was done using a traditional camera and by a micro-CT scan. The wick structure is composed of 6 layers of screen mesh. From the inside of the heat pipe, one layer of a 100-mesh screen, three layers of 400-mesh screens, and two layers of 60-mesh screens were rolled to compose the wick structure. As will be shown, this design decision was informed by the mesh composition determined to have the most favorable performance characteristics determined by the results of the wick characterization experiment. To fabricate the wick structure, mesh screens were wrapped around a 1.2 m long rod with a diameter of 17.46 mm (11/16 inches). The cylindrical shape of the wick structure was retained by spot welds along the axial direction with 1.5 ~ 2.0 mm intervals. After removing the rod, the wick structure was inserted into a 1.2 m 304 L seamless stainless steel pipe with an outer and inner diameter of 25.4 mm and 22.1 mm, respectfully. The dimensions of the manufactured wick are 18.1 mm of inner diameter, 1.12 mm of thickness, and 20.3 mm of outer diameter, which leaves 0.95 mm of the gap between the inner surface of the stainless tube when inserted. The gap between the wick structure and the inner wall of the tube was maintained by wire-wrapping each end of the wick structure.

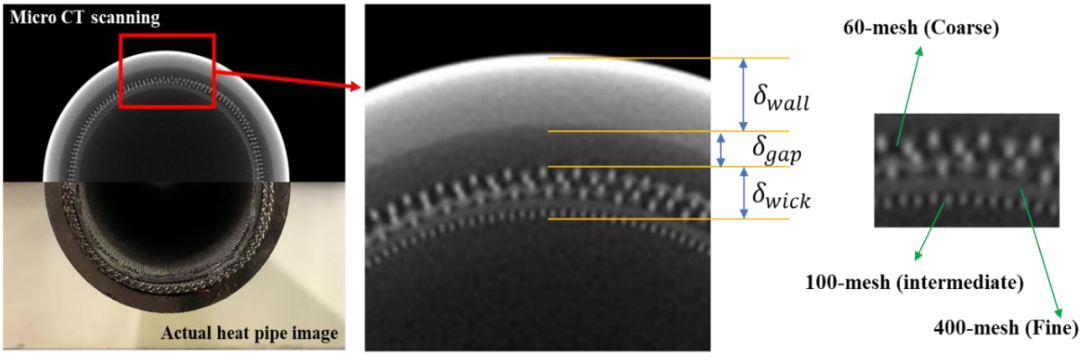

Figure 12. The cross-sectional design of the wick structure inside the heat pipe taken by micro-CT scanning

Heat pipe fabrication consists of cleaning, vacuuming, fluid filling, and sealing processes. The inside of the stainless-steel pipe and wick structure was cleaned using ethanol. Each end of the pipe was closed using compression fittings. One side of the pipe was connected to the vacuum pump and working fluid insertion system. After -90 kPa of vacuum pressure was achieved by the vacuum pump, 160 mL of DI water was inserted into the pipe as a working fluid. Then, the pipe was sealed by a locking ball valve connected to the vacuum pump. As a final step of the fabrication, leakage was checked to verify the condition inside the heat pipe.

2.3.2. Heat Pipe Performance Experimental Facility

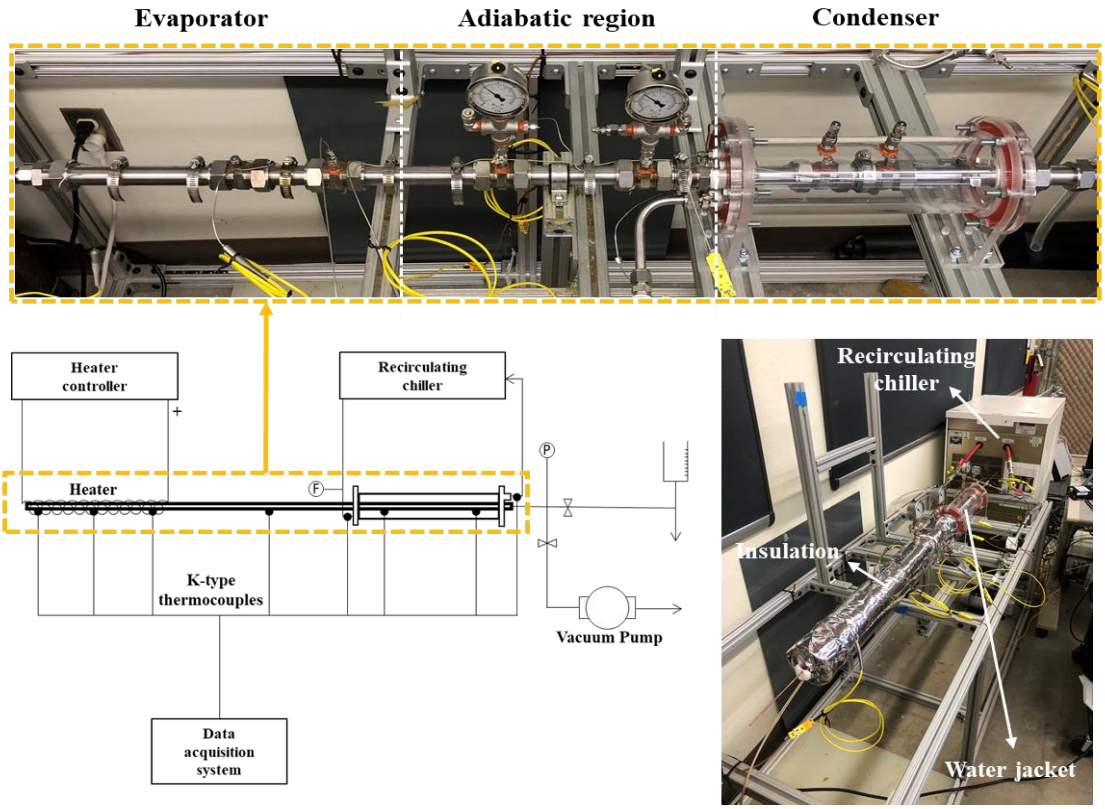

Figure 13. The schematic and the picture of the heat pipe experimental setup

Figure 13 shows the schematic and a picture of the heat pipe experimental setup. The experimental setup consists of three parts, the heat pipe, the heating & cooling regions, and the measurement system. The 1.2 m stainless steel heat pipe with an annular multi-layered composite screen mesh was fixed with a horizontal geometry. The length ratio of the evaporating, adiabatic, and the condensing region was set as 1:1:1. A heating coil with 468 W of maximum power was wrapped on the evaporator section of the heat pipe. The heater was connected to a transformer and power meter to control the power output and the heater was wrapped in a copper tube for uniform heat transfer to the heat pipe as shown in Figure 14. A water jacket with a variable flow rate was installed at the condensing region of the heat pipe to remove the heat transferred by the heat pipe. The inlet temperature of the cooling fluid inside the water jacket was controlled by a Merilin M33 chiller from the Neslab company. The inlet and outlet temperatures were measured using K-type thermocouples and the flow rate was measured using a flow meter to monitor the energy balance of the heat pipe module. Evaporating and adiabatic regions of the heat pipe were insulated using glass wool with a thickness of 50 mm.

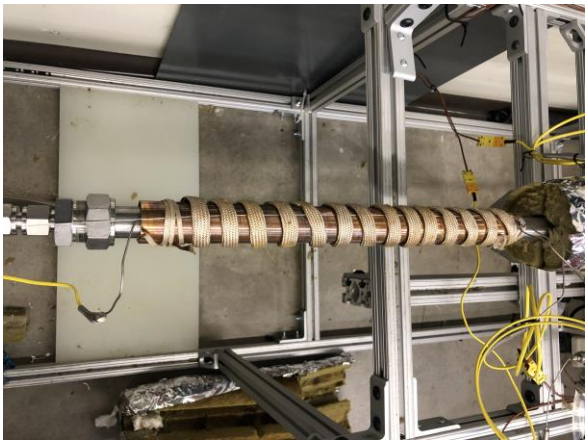

Figure 14. A heater is wrapped around the copper tube on the evaporator section.

The temperature distribution along the outer surface of the heat pipe was measured using K-type thermocouples. Three thermocouples were attached to the outer surface of the evaporator region, and one thermocouple was fixed in the middle of the adiabatic region. Two thermocouples were inserted into the water jacket and their endpoints were fastened to the outer surface of the heat pipe. To monitor the inner pressure, four analog pressure gauges were used. Four pressure gauges, one at the evaporator region, two at the adiabatic region, and one at the end of the condenser region, were installed along the heat pipe.

2.3.3. Experimental Conditions

The heat pipe performance experiment was designed to evaluate the capillary limitation of the heat pipe, a key parameter that defines the heat removal capabilities of a heat pipe at a given temperature. Inside the heat pipe, the liquid which condensates in the condenser is passively returned to the evaporator by the capillary force of the wick structure. The capillary limitation is the maximum power that the heat pipe can carry while keep returning the condensate by capillary force. Thus, the capillary limitation of a heat pipe can be calculated from Eq. 6 which explains the amount of the power that the capillary force no more overcomes the pressure drop due to gravity, liquid flow, and vapor flow.

$$Q_{capillary} = \frac{2\sigma}{r_{eff}} \frac{KA_{wick} h_{lv} \rho_l}{\mu_l L_{eff}} = \frac{K}{r_{eff}} \frac{2\sigma A_{wick} h_{lv} \rho_l}{\mu_l L_{eff}} \qquad \textbf{Eq. 6}$$

Here, h_{lv} is the latent heat of the working fluid, and L_{eff} is the effective length of a heat pipe which can be calculated from Eq. 7.

$$L_{eff} = 0.5L_E + L_A + 0.5L_C \qquad \textbf{Eq. 7}$$

where, L_E, L_A, and L_C presenting the length of the evaporator, adiabatic region, and condenser of the heat pipe, respectively. In Eq. 6, the pressure drop due to the vapor flow is assumed to be negligibly small, and the heat pipe is in the horizontal position so that the gravitational pressure drop is also negligible.

This study controls two boundary conditions: the operating temperature and input power. The operating temperature is controlled from 50 ℃ to 80 ℃ by adjusting the temperature and flow rate of the coolant traveling through the water jacket. The power imposed on the evaporator section of the heat pipe is controlled and monitored using a transformer and power meter. The range of the heating power is set from 100 W to 400 W. The ranges of the boundary condition are selected considering the geometry of the heat pipe and the properties of the working fluid. This study focuses on the hydraulic parameters of the mesh structure, such as porosity, permeability, and effective pore radius. Since the capillary limitation is highly affected by those parameters, the expected range in which the capillary limitation might occur is selected based on the calculation result of Eq. 6.

2.3.4. Experimental Procedure

The experimental procedure to measure the heat transfer performance of the heat pipe was performed as follows: First, the targeted heating power is applied to the evaporator region. The heating power increases both the heat pipe's surface temperature and operating temperature. Here, the operating temperature of the heat pipe can be indicated by the temperature of the vapor in the vapor core which is the same as the surface temperature of the adiabatic section. The temperature and the flow rate of the coolant

traveling in the water jacket are controlled to adjust the operating temperature of the heat pipe. For example, suppose the operating temperature exceeds a specified value. In that case, a coolant with a lower temperature and higher mass flow rate is provided to the water jacket to reduce the internal pressure of the heat pipe. After both heating power and operating temperature reach the targeted values, steady-state is determined by checking the temporal variation of the surface temperature. During a steady-state, temperature and pressure are measured for 5 minutes. Then, the heat input is increased to the next level and repeated the same procedure.

An experiment is performed to determine the operating limitation by increasing the power input while maintaining the operating temperature until the limiting condition is found. The point at which the operating limitation is reached is indicated by monitoring the surface temperature of the heat pipe. The temperature of the evaporator region starts to rise rapidly when the heat pipe meets the operating limit due to a loss of heat transfer caused by dry out. To prevent the failure of the experimental setup, the heating was shut down when a rapid increase in the temperature was observed, and the boundary condition was marked as an operating limitation point.

2.3.5. Temperature Distribution Measurement

Other than operating limitation models, modeling the start-up behavior of the heat pipe is an important topic, especially for its application to the microreactor. Change of heat pipe's temperature is one of the key parameters for developing and validating heat pipe models. Generally, the temperature change at a point is measured using a thermal couple as a traditional temperature measurement method. However, in this experiment, a

novel temperature measuring device is used to acquire a linear distribution of temperature across the whole heat pipe. The Optical Distributed Sensor Interrohators (ODiSI) system is used to measure the inside/outside temperature of the heat pipe. The ODiSI system can measure and acquire strain and temperature with a spatial resolution of up to 0.65 mm, enabling the mapping of highly detailed strain and temperature profiles. High-definition fiber optic sensing (HD-FOS) is a distributed sensing technology based on the naturally occurring Rayleigh backscatter in optical fiber. It delivers maximum spatial resolution for static and quasi-static applications. Figure 15, and Figure 16 show the overall system configuration and a picture of FOS

ODiSi controller with application software | Mainframe with 8 channels | Remote modules connect sensors to mainframe

Figure 15. Overall OdiSI system configuration

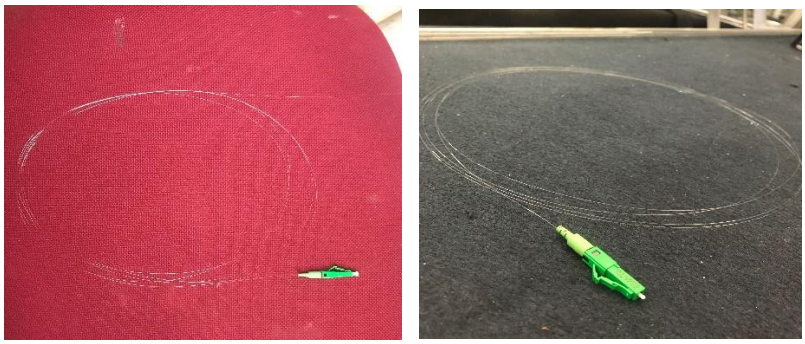

Figure 16. Fiber optic sensor(FOS)

The ODiSI system can operate up to eight fiber optic sensor channels and measure temperatures with sensor lengths up to twenty meters per channel. The measurement rate is 40 Hz for a single channel five meters sensor mode. The temperature measurement resolution is 0.1 °C, and the measurement range is from -40 to 200 °C. The temperature sensor is polyimide-coated fiber in the Polytetrafluoroethylene (PTFE) tube, and its measurement uncertainty is 0.9 °C which is equal to twice the standard deviation calculated from a set of 1000 measurements. As shown in Figure 17, FOS is installed in a variety of locations, including the exterior of the heat pipe, the gap between the tube and the wick, the inner mesh surface, and the heat pipe's core. These sensors allow for precise measurement of the overall temperature distribution at each place and visual observation of the heat pipe's temperature change.

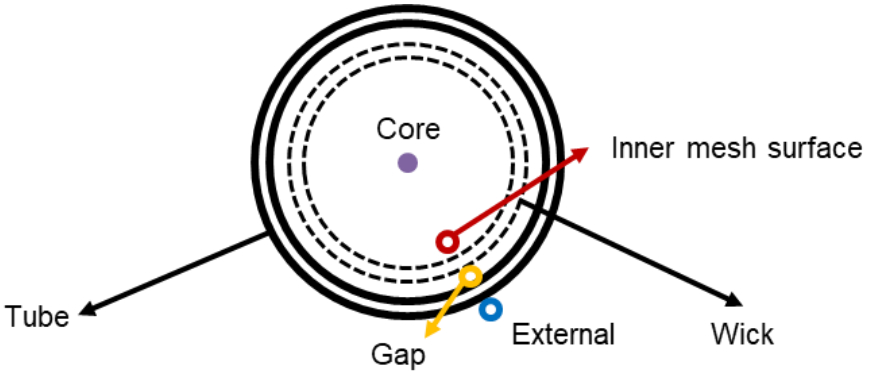

Figure 17. FOS measurement location in the heat pipe.

2.4. Heat pipe Visualization Experiment

2.4.1. Heat Pipe Construction

This study is simply focusing on seeing and recording the inside of the heat pipe rather than conducting sophisticated thermodynamic analysis of what is happening. To

begin, a half-round circle annular wick structure was created as illustrated in Figure 18 in order to visualize the boiling pattern inside the heat pipe. We recorded the top and bottom views of the half wick heat pipe. After that, the whole annular wick heat pipe was constructed the inside of the heat pipe, just six layers of 100-mesh screens were rolled to compose the wick structure. To fabricate the wick structure, mesh screens were wrapped around a 1.2 m long rod with a diameter of 17 mm. Spot welds retained the cylindrical shape of the wick structure along the axial direction with 1.5 ~ 2.0 mm intervals. After removing the rod, the wick structure was inserted into a 1.2 m borosilicate seamless glass tube pipe with an outer and inner diameter of 25.4 mm and 19.9 mm, respectively. The dimensions of the manufactured wick are 18.8 mm of inner diameter, 0.49 mm of thickness, and 19.29 mm of outer diameter. There is no wire-wrapping at the end of the wick structure to maintain a particularly constant gap like the previous wick of the heat pipe experiment. Heat pipe fabrication consists of cleaning, vacuuming, fluid filling, and sealing processes. The inside of the glass tube pipe and wick structure was cleaned using ethanol. Each end of the pipe was closed using compression fittings. One side of the pipe was connected to the vacuum pump and working fluid insertion system. After -90 kPa of vacuum pressure was achieved by the vacuum pump, 240 mL of DI water was inserted into the pipe as a working fluid. Then, the pipe was sealed by a locking ball valve connected to the vacuum pump. As a final step of the fabrication, leakage was checked to verify the condition inside the heat pipe.

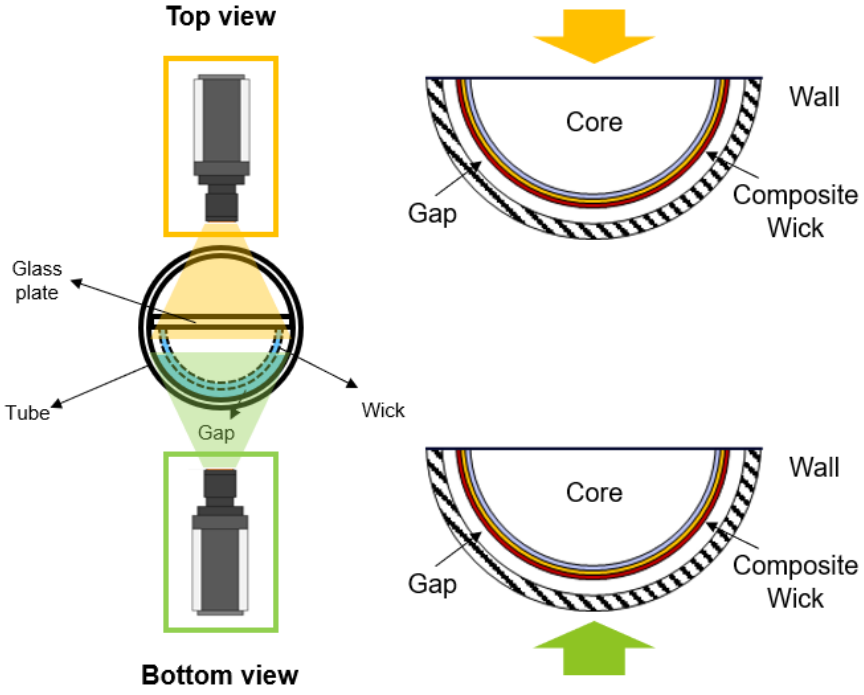

Figure 18. Experimental setup to see the boiling pattern inside heat pipe

2.4.2. Heat Pipe Visualization Experimental Facility

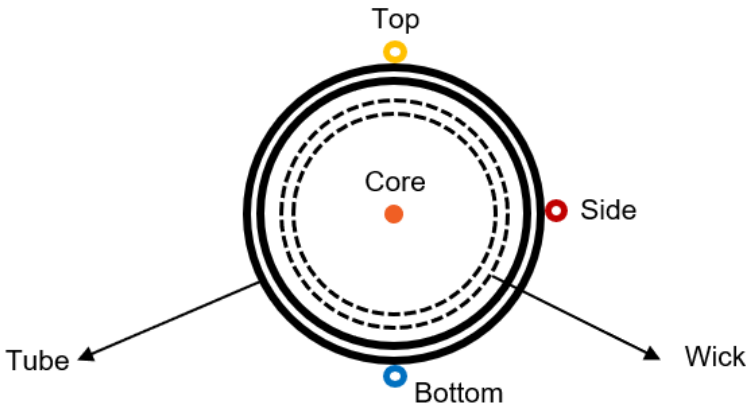

Figure 19. FOS measurement location in the heat pipe visualization experiment.

In the heat pipe visualization experiment, the FOS is simply located as shown in Figure 19. This is because the working fluid is mainly at the bottom due to gravity, it was expected that there would be a temperature difference between the top and the bottom.

The flow of fluid inside the heat pipe was visually observed in this experiment. In particular, the boiling phenomena occurring in the evaporator section and the temperature change associated with it were primarily monitored. Because this experiment emphasizes visual observation of the heat pipe's interior phenomena rather than thermal or hydrodynamic analyses, we concentrated on establishing observation equipment capable of viewing this well.

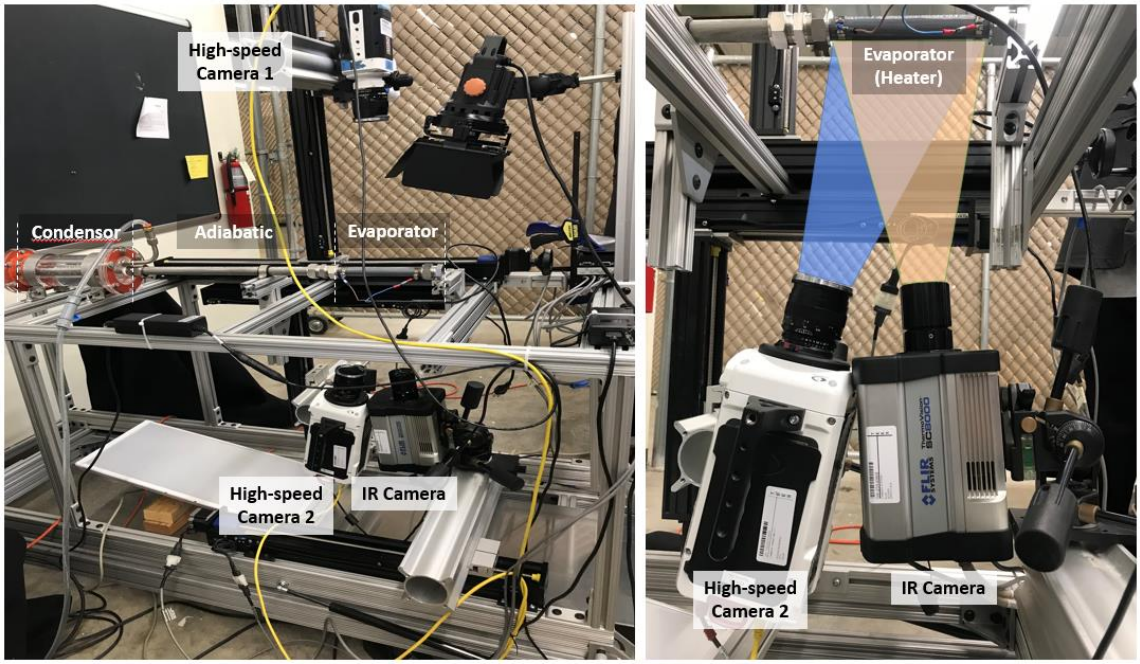

Figure 20. Heat pipe visualization experimental setup

Figure 20 shows the picture of the heat pipe visualization experimental setup. The experimental setup consists of three parts, the heat pipe, the heating & cooling regions, and the measurement system similar to the previous stainless steel heat pipe experimental setup. However, the pipe is replaced with a clear glass tube, including a transparent heater, which allows a fully visualized heat pipe experiment. The 1.2 m glass heat pipe with an annular multi-layered screen mesh was fixed with a horizontal geometry. In addition, as

shown in Figure 21, the experimental setup can be inclined with the four gas pressure springs and some frame connectors that can make the inclination so that the entire device can be set angle from 0 to 90 degrees. A transparent heater, the evaporator section of the heat pipe, is connected to a direct current power supplier with a maximum output of 3 kW. A water jacket with a variable flow rate was installed at the condensing region of the heat pipe to remove the heat transferred by the heat pipe. The inlet temperature of the cooling fluid inside the water jacket was controlled by a Merilin M33 chiller from the Neslab company. To examine the boiling phenomenon and fluid flow in the heater more precisely, high-speed cameras are mounted at the top and bottom. An infrared camera is installed at the bottom to monitor the temperature change of the heater.

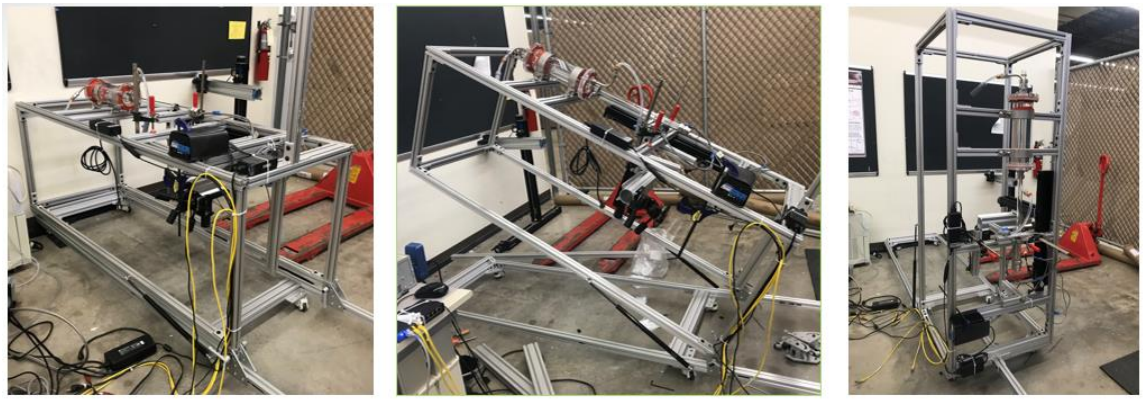

Figure 21. Incline-enabled heat pipe visualization experimental setup

2.4.3. Experimental Conditions

In the heat pipe visualization experiment, the high-speed camera and infrared camera are used to observe and record the heater within the heat pipe. After maintaining steady power to the heater, and the heat pipe reaches a stable condition, shooting with the high-speed camera and the infrared camera begins. Adjust the infrared camera to 100

frames per second and be ready to shoot simultaneously with the high-speed camera. To achieve a clear image, halogen light is mounted on the top side of the experimental equipment, and an LED lamp is mounted on the underside. For the heat pipe, the experiment begins with the device at a 0-degree inclination, and after completing the 0-degree experiment, the same experiment is repeated at 45 and 90 degrees. Throughout the experiment, the cooler constantly supplied the coolant with 10 degrees Celsius.

2.4.4. Experimental Procedure

Before turning on the heat pipe, set the cooler to a temperature of 10 degrees to chill the condenser region. The top and bottom high-speed cameras focus on the wick inside the heat pipe and adjust the angle so that the heater, which is the evaporator section of the heat pipe, appears on the camera screen as a whole. Before shooting, the infrared camera is calibrated. The camera angle is adjusted so that the evaporator section of the heat pipe appears in the camera as a full screen, similar to the high-speed camera. Begin operating the heat pipe by increasing the heater's power and heat, and then gradually increase the power in steps of 25W, 50W, 100W, and 150W. Hold for 1 hour or more at the first 25W power level and at least 30 minutes at the subsequent power level. While the heater is powered on, only the infrared camera is set to 1fps for 30 minutes of shooting, and the high-speed camera is turned off. After stabilizing the heat pipe by maintaining it at each set power level for a specified period, begin shooting. The upper/lower part's high-speed camera is set to 200 frames per second, while the infrared camera is set to 100 frames per second. Both cameras simultaneously record the flow of fluid inside the evaporator section and its temperature at the corresponding power for 80 seconds. When

it is determined that the heater has reached its operating temperature, it is eventually turned off after additional shooting with a high-speed camera and infrared camera and slowly cooled with natural cooling. While the heater is being powered on, only the infrared camera is set to 1fps for 30 minutes of shooting, and the high-speed camera is turned off. After stabilizing the heat pipe by maintaining it at each set power level for a specified period, begin shooting. The upper/lower part's high-speed camera is set to 200 frames per second, while the infrared camera is set to 100 frames per second. Both cameras simultaneously record the flow of fluid inside the evaporator section and its temperature at the corresponding power for 80 seconds. When it is determined that the heater has reached its operating temperature, it is eventually turned off after additional shooting with a high-speed camera and infrared camera, and slowly cooled with natural cooling.

3. RESULT AND DISCUSSION[*] [**]

3.1. Wick Characterization Experimental Result

3.1.1. Experimental Comparison for Various Composite Wick

Results of the wick characterization experiments for 9 types of multi-layered screen meshes are shown in Table 2. The porosities of each mesh, determined by the mesh saturation experiment, were used in Eq. 3 to determine the permeability and effective pore radius. Figure 22 presents the result of the mean absolute percent deviation between time values of the data set and calculated time using Eq. 3 for case #8. Deviations calculated from five pairs are summed up and presented on the left side of Figure 22. The plane of the deviation in the sample space of permeability and effective pore radius has a shape of a trough. From the side views of the plot shown in the middle and the right side of Figure 22, a point with the minimum deviation can be identified and its respective permeability and effective pore radius were selected as the true value. The composite wick case #8, for example, is determined to have a permeability of $0.635 \times 10^3 \mu m^2$ and a 0.169 mm effective pore radius.

[*] Reprinted with permission from "An experimental investigation on the characteristics of heat pipes with annular type composite wick structure" by Joseph Seo, Daegeun Kim, Hansol Kim, and Yassin Hassan, 2022, Nuclear Engineering and Design, vol. 390, 111701, copyright 2022 by Elsevier B.V. All rights reserved.

[**] Reprinted with permission from "Design Optimization of Gap Distance for the Capillary Limitation of a Heat Pipe with Annular-Type Wick Structure" by Joseph Seo, Daegeun Kim, Hansol Kim, and Yassin Hassan, 2022, Physics of Fluids, vol. 34, 067116, copyright 2022 Author(s). Published under an exclusive license by AIP Publishing.

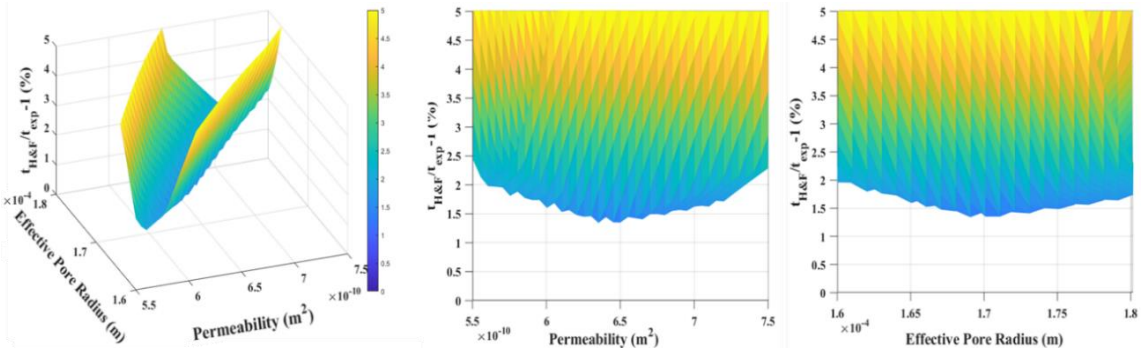

Figure 22. The result of the mean absolute percent deviation between time values of the data set and calculated time in a sample space of permeability and effective pore radius

Table 2. Result of the wick characterization experiment for various types of multi-layered screen meshes.

Case #	Total number of layers	Mesh composition			Measurement result			
		100-mesh (inside layer)	400-mesh (middle layer)	60-mesh (outside layer)	Porosity (ε [−])	Permeability (K [μm^2])	Effective Pore Radius ($r_{eff}[mm]$)	$\frac{K}{r_{eff}}$ [μm]
1	6	6	0	0	0.642	0.815×10^3	0.266	3.064×10^3
2		0	6	0	0.767	0.825×10^3	0.232	3.556×10^3
3		0	0	6	0.626	0.745×10^3	0.419	1.778×10^3
4		2	2	2	0.634	0.985×10^3	0.252	3.909×10^3
5		1	3	2	0.653	1.435×10^3	0.213	6.737×10^3
6		2	3	1	0.667	1.205×10^3	0.264	4.564×10^3
7		2	1	3	0.637	0.300×10^3	0.188	1.596×10^3
8		3	2	1	0.671	0.635×10^3	0.169	3.757×10^3
9		3	1	2	0.682	1.080×10^3	0.284	3.803×10^3

Like in the case of the porosity measurement, the uncertainty of the measurements is quantified by repeating the same procedure and by checking the amount of the deviation. The experimental procedure starting from constructing the wick assembly with a single

type of wick structure and fixed gap distance is repeated 27 times and the deviation of the permeability calculation is calculated. As a result, the data has $\pm$4.71% of standard deviation when they are compared with the average value.

Experimental results show that mesh case #2, which was built with 6 layers of the finest mesh (400-mesh), has the highest porosity, the lowest permeability, and the smallest pore radius. This is consistent with the geometric characteristics of the mesh. Among the three types of screen meshes used in this study, the 400-mesh has the highest porosity and the smallest pore size, and the lowest permeability. On the other hand, mesh case #5 has the highest permeability.

From Eq. 6, it can be recognized that the value of K/r_{eff} determines the capillary limitation of the heat pipe when the other geometric parameters and liquid properties are the same. In this study, therefore, the value of K/r_{eff} is checked as a parameter of interest for the wick performance. From Table 2, it can be noticed that composite mesh case #5 is expected to provide the highest capillary limitation when it is installed inside the heat pipe. Because the geometry of the composite wick structure is not homogeneous, the phenomena that occur inside of it are complex and highly unpredictable. This results in a lack of an analytical model to optimize the design of the wick structure. In this study, therefore, several samples of wick structures were built, and their hydraulic parameters were measured by relatively simple experimental methods. As will be shown by the results from the heat pipe performance experiment, these measured parameters can be effectively used to predict the operating limitations of a heat pipe.

3.1.2. Verifying the Gap effect

The investigation of the effect of the gap between the wick and the wall was conducted by measuring the performance of a wick structure with different gap sizes. Mesh case #5 was selected as a testing sample since it showed the best performance among different combinations of multiple screen meshes. From Eq. 3, multiple pairs of experimental data for the mass (m_{exp}) and the time (t_{exp}) are required to find the two unknown variables, permeability (K) and the effective pore radius (r_{eff}). If only a single pair of the data is used, on the other hand, one could not obtain the solution of the equation but can still check the relationship between the permeability and the effective pore radius. Figure 23 shows the line on the sample space of permeability and the effective pore radius which results in a solution to Eq. 3. These lines were determined using a single pair of the data measured at $t = 5s$. The lines which indicate the relationship between the two parameters show the performance of the mesh. Based on the discussion above, K/r_{eff} is an important parameter of the mesh when the capillary limitation of the heat pipe is considered. In the same perspective, the slope of the lines in Figure 23 might be an indicator of the wick performance. For example, wicks with 0.7 mm and 1.2 mm of gap distance from the wall show the smallest slope in the plot which means the largest K/r_{eff} value. On the other hand, the bare mesh without any wall shows the smallest K/r_{eff} value, inferring the lowest performance.

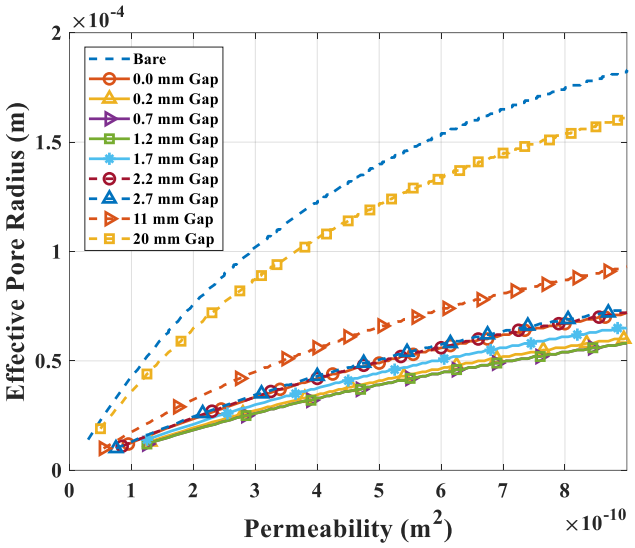

Figure 23. The relationship between permeability and effective pore radius of the wick structure with varying gap distance.

As mentioned above, a unique solution of the permeability and effective pore radius can be found when multiple pairs of data are used. In the ideal case, a single line on the sample space will be created for each pair of mass and time data, and lines will be crossed at a point, which is a unique solution. Thus, even though the lines in Figure 23 are calculated using only a single pair of data, the actual permeability and effective pore radius values of the mesh with various gap distances lay on the line. In this point of view, a lower effective pore radius and a higher permeability could be expected for the mesh with 0.7 ~ 1.2 mm of gap distance compared to the bare mesh. This approach might be meaningful because obtaining a solution for Eq. 3 is achieved by an iterative method and bringing more pairs of data into the calculation increases the computational cost linearly. The result from only one pair of data could provide valuable intuition about the performance of the wick structure while reducing the time required to determine a more exact solution. This

may be especially useful for a study focused on the comparison of multiple wicks where computational costs would quickly increase.

Figure 24 shows the result of the calculations with 5 pairs of mass and time data collected from the experiment. Unlike the results with a single pair of data introduced above, a point that has the minimum mean absolute percent deviation can be found in the space of permeability and effective pore radius. To investigate the effect of the gap distance on the two parameters, the results are plotted against the gap distance. In the plot on the left side of the figure, the permeability increases as the gap become wider, with a peak at a gap distance of 1.2 mm. As the gap increases more, the permeability can be seen to become smaller and converge to the bare mesh case. On the other hand, the effective pore radius is shown to behave inversely to the pore radius in the right figure. The effective pore radius become smaller as the gap increases with a peak at 0.7 mm of distance.

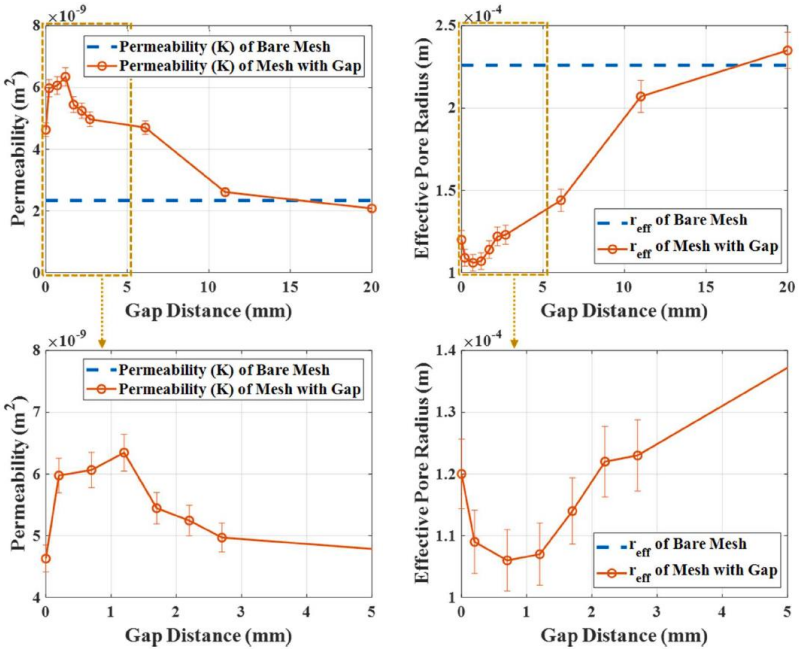

Figure 24. The result of permeability (left) and effective pore radius (right) measurement of the wick structure with varying gap distance.

An interesting point can be found from the results of the 0 mm gap case. Considering that a wick with higher permeability and smaller effective pore radius has better performance, the mesh with a 0 mm gap can be noticed to have better performance than the bare mesh case. This is because the geometry of the screen mesh creates micro-channels even though it is attached to the wall. These channels provide extra capillary pressure and flow paths for the fluid. The large difference with bare mesh emphasizes the necessity of further studies on the impact of wall effects on heat pipe performance.

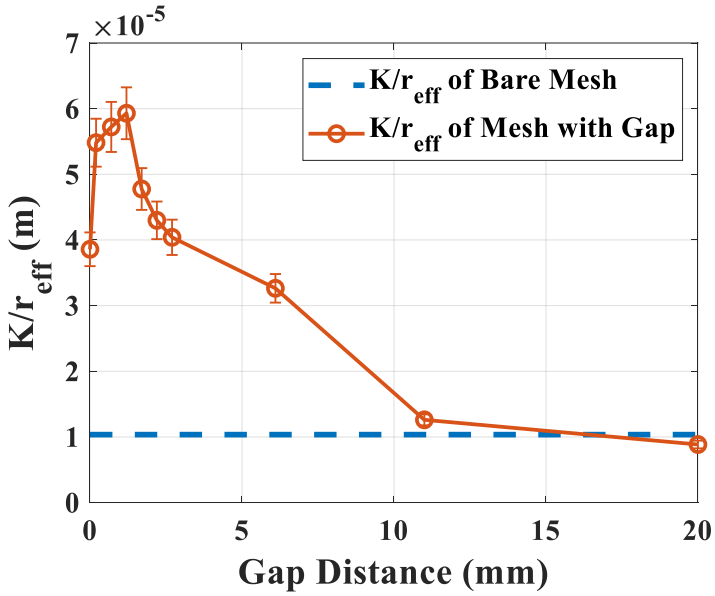

Figure 25. The result of K/r_{eff} measurement of the wick structure with varying gap distance.

The result of the K/r_{eff} calculation is plotted against gap distance in Figure 25. An increasing trend from 0 mm to 1.2 mm and a decreasing trend from 1.2mm to 20 mm with convergence to bare mesh results was observed. The enhancement of the performance gained by the gap can be explained in two ways. First, additional capillary pressure is created by the gap. Since the space between the inner surface of the tube and the outer

surface of the mesh structure consists of a narrow cylindrical channel, extra capillary pressure is generated and reduces the effective pore radius from an axis-symmetric form of the Laplace-Young equation which is as follows:

$$\Delta P_{capillary} = \frac{2\sigma\cos\theta}{r} = \frac{2\sigma}{r_{eff}} \qquad \textbf{Eq. 8}$$

Second, the channel created by the gap provides an additional flow path for the working fluid which reduces the pressure drop. The reduced pressure drop is reflected in the increased permeability of the wick structure. From the explanation above, it can be seen that the two effects become competing factors to one another when they are explained using gap distance. The additional capillary pressure from the gap is maximized when the smallest gap distance is introduced. This can be easily recognized from Eq. 8. On the other hand, the pressure drop due to the shear stress of the channel is reduced when the diameter of the channel, the gap distance in this study, is increased. Due to this trade-off of two benefits, there must be an optimal gap size to produce the largest benefit to heat pipe performance. In this study, the optimal gap distance which gives the best wick performance was experimentally found to be 1.2 mm. This value only includes effects on hydraulic characteristics of the wick structure, not on thermal characteristics of the wick. The gap might increase the thermal resistance in the radial direction of the heat pipe when a working fluid with low thermal conductivity is used. This impact may be less significant in real scenarios as annular type multi-layered composite screen mesh heat pipes are mainly used with high conductivity liquid metals as the working fluid. The experimental data provided in this study which relates to the optimal gap distance may be of value as it has not been addressed in current literature.

3.2. Capillary Rise and Contact Angle Experimental Result

3.2.1. Capillary Rise Experiment Results

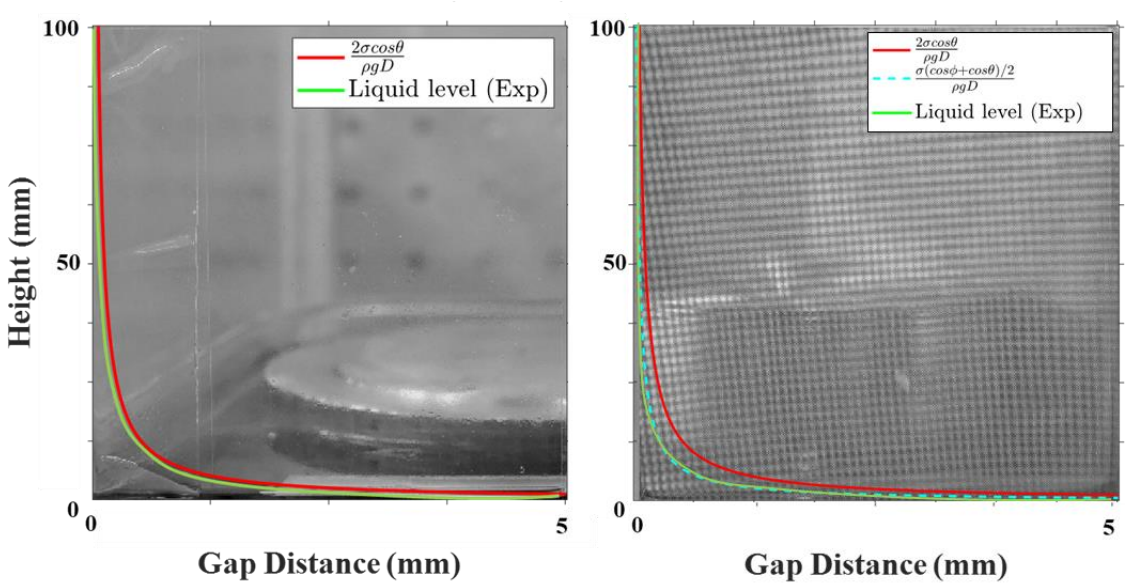

Figure 26. Comparison between the experimental capillary rise and prediction from theoretical calculations (left: solid-solid surface, right: solid-mesh surface)

Figure 26 shows the experimental result of the rising height measurement. In the graph, the x-axis represents the gap distance between the two plates, and the y-axis represents the height of capillary rise. By substituting the contact angle measurement result into Eq. 5, the theoretical capillary rising curves were obtained, which are shown in terms of the liquid level. It must be noted that Eq. 5 can be applied not only to the case of the solid-solid surface but also to the case of the solid-mesh surface. The contact angle of a liquid against porous media is determined by the natural characteristics of the material and the capillary action due to the geometry of the media. For example, a porous media consisting of hydrophilic materials provides a smaller contact angle with water. However, if the structure of the media causes high capillary pressure, the liquid pulling (or spreading) effect decreases the contact angle. These phenomena occurring on the surface of porous

media may affect the height of capillary rise of the liquid in the gap between the solid and mesh surface. An important result obtained from this experiment was that these complicated effects could be explained by the contact angle information and that Eq. 5 could be used to accurately predict the height of capillary rise in such cases.

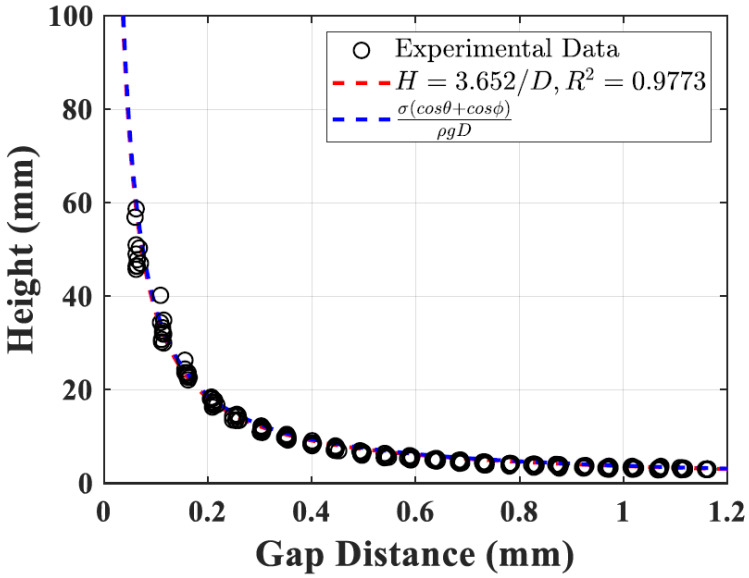

Figure 27. Uncertainty analysis of rising height measurement.

Data extraction from images was conducted to perform uncertainty analysis. The measurement procedure was repeated 13 times from immersing to drying the sample structure. The extracted data points from 13 measurements were plotted on a plain of gap distance and rising height, as shown in Figure 27. Based on the consideration of the form of the Laplace-Young equation, a curve fitting was performed using a power function with -1 of an exponent. As a result, a curve with 3.652 of the constant was fitted. The rate of variance (or R^2 value) was determined to be 0.9773, and ± 2.27% was selected as an uncertainty of the measurement. The fitted curve was then compared with the calculation result of Eq. 5. These two curves almost overlap, as shown in the plot. The correspondence

becomes more clear when the constant of equations is compared. The constant of the Laplace-Young equation can be calculated by substituting the properties of ethanol for the product term, $(\sigma(cos\theta + cos\varphi)/\rho g)$, in front of 1/D. The calculation results in 3.7634, which results in a 2.24% of discrepancy. As a result, it is noted that Eq. 5 can be applied not only to the case of the solid-solid surface but also to the case of the solid-mesh surface which allows a large possibility of extension to heat pipe application.

3.2.2. Verification of Curvature Effect

The capillary rise in the curved surface was projected onto the plane using an angle reference line and compared to the capillary rise in the plane surface, as shown in Figure 28. The data points extracted from the image of the experiment are marked as black circles. As with the flat surface cases, the uncertainty was checked by repeating the experiment 13 times. The curve fitting with -1 of exponent resulted in a constant value of 3.743. The rate of variance (or R^2 value) was determined to be 0.9401, and the measurement was considered to have ±5.09% of uncertainty from it. The larger uncertainty compared to the flat case might be caused by the complexity of the experiment due to the curved surfaces. As abovementioned, the constant of the Laplace-Young equation calculated from the properties of ethanol is 3.7634. There is only a 0.54% discrepancy between the two constants. As a result, it seems there is no or negligible curvature effect on the rising height between mesh surface and solid surface, which means the correlation could be used to accurately predict the height of capillary rise, even in the case of curved geometry. Although further investigation is required on the effect of varying curvatures, the curvature effect may be ignored for the heat pipe. This is because the typical design of

heat pipes for micro reactors considers a diameter range between 25.4 and 31.8 mm, which is similar to that in our experiment.

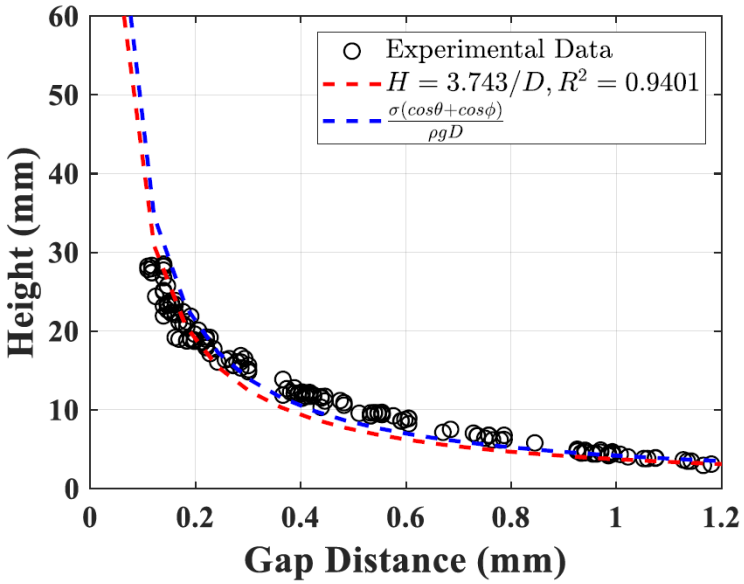

Figure 28. Comparison of capillary rise between curved and flat surfaces

3.2.3. Investigation of the Gap Effect on the Capillary Limitation of the Heat Pipe

As mentioned above, the objective of the study is to determine the effect of the gap size on the performance of the annular wick type heat pipe. In the annular wick-type heat pipe, the gap between the wick and wall increases the performance of the heat pipe, specifically the capillary limitation, which is a crucial operating limitation of the heat pipe.

The improvement in performance owing to the gap can be explained in two ways. First, the gap creates additional capillary pressure, which reduces the effective pore radius in an axis-symmetric form of the Laplace–Young equation, as the space between the inner surface of the tube and the outer surface of the mesh structure is a narrow cylindrical channel. Second, the channel created by the gap provides an additional flow path for the

working fluid, thereby reducing the pressure drop. The increased permeability of the wick structure reflects this reduced pressure drop.

Therefore, considering the aforementioned effects from the perspective of gap distance, they become competing factors. When the smallest gap distance is introduced, the additional capillary pressure from the gap is maximized. However, the pressure drop caused by the shear stress of the channel decreases as the diameter of the channel, or the gap distance in this study, increases. On account of this trade-off between the two benefits, an optimal gap size may exist that produces the greatest benefit to heat pipe performance. In the previous discussion, the optimal gap distance for the best wick performance was determined experimentally to be 1.2 mm by comparing K/r_{eff} values of the wick with varying gap distance. They performed a set of experiments on a mesh sample consisting of a stainless-steel plate and wick structure, as shown in Figure 5. The mass of the liquid pulled up by the mesh was measured according to the time, as shown in Figure 6. To calculate permeability and effective pore radius from the experimental data, the method suggested by Holley and Faghri (Holley & Faghri, 2006) was used, and this method was already introduced in Eq. 2. By performing the same measurement with varying gap distances, they suggested the gap distance with the largest K/r_{eff} (Figure 25) which can be directly referred as a gap design for the annular wick type heat pipe with the highest capillary limitation prediction.

However, the study did not provide analytical support for the experimental results which are tried in this study using the contact angle modeling performed in the previous section. To analytically explain the gap effect on the wick structure, the value of K/r_{eff}

in a narrow gap between solid surface and mesh surface should be quantified. Thus, the first step to theoretically analyze the gap effect was to obtain the analytical data set of the height of the capillary rise of the liquid between the stainless-steel plate and mesh plate over time, at a different gap distance to solve the Eq. 2. In 2008, Higuera et al. (Higuera et al., 2008) suggested a non-dimensional equation for calculating a temporal change in the height of capillary rise between two solid plates. They started with the Reynolds equation of lubrication theory (C. K. Batchelor and G. Batchelor, 2000).

As shown in Figure 7, the intersection of the liquid surface and the symmetry plane bisecting the wedge is sought in the form $z = H(x, t)$. Normalization was performed by scaling x, z, and H with H_c, P with $\rho g H_c$, respectively, and the time with t_c, where H_c and t_c were defined as follows:

$$H_c = \left(\frac{2\sigma cos\theta}{\rho g \alpha}\right)^{\frac{1}{2}},\ t_c = \frac{12\mu}{\rho g H_c \alpha^2}. \qquad \textbf{Eq. 9}$$

Here, μ is the dynamic viscosity of the fluid. Resultantly, the governing equations are as follows:

$$\frac{\partial}{\partial x}\left(x^3 \frac{\partial P}{\partial x}\right) + x^3 \frac{\partial^2 P}{\partial z^2} \qquad \textbf{Eq. 10}$$

in $x > 0, 0 < z < H(x, t)$, where P is:

$$P = -\frac{1}{x} + H \qquad \textbf{Eq. 11}$$

and H is:

$$\frac{\partial H}{\partial x} - x^2 \frac{\partial P}{\partial x}\frac{\partial H}{\partial x} + x^2 \frac{\partial p}{\partial z} = 0 \qquad \textbf{Eq. 12}$$

For the boundary,

$$P = 0 \text{ at } z = 0 \quad \textbf{Eq. 13}$$

$$x^3 \frac{\partial^2 P}{\partial z^2} \to 0 \text{ when } x \to 0 \quad \textbf{Eq. 14}$$

$$H = 0 \text{ when } x \to \infty \quad \textbf{Eq. 15}$$

Here, Eq. 12 was introduced to explain the modification of the pressure at the surface by the sum of the capillary depression. Based on the assumption that $\partial^2 P/\partial z^2$ in the Eq. 10 become 0 for $t \ll 1$, Higuera et al. suggested the solution of the equation with the initial condition $H_i = 0$, as follows:

$$xH + \ln(1 - xH) = -x^3 t \quad \textbf{Eq. 16}$$

The approximation of the early-stage evolution ($t \ll 1$) and the solution are applicable to the calculation of the permeability and the effective pore radius (Eq. 2) because the temporal derivation of the height of capillary rise at the early stage obtained from the experiment is used for the calculation (Holley & Faghri, 2006).

It must be noted that Higuera et al. suggested the solution for the case of two solid plates. To utilize the solution for this study, which considers a similar experimental approach but different surface conditions, that is, solid–mesh plates, the scaling factor must be modified. This was achieved by introducing the result of the contact angle experiment from the previous section as follows:

$$H_c = \left(\frac{2\sigma cos\theta}{\rho g \alpha}\right)^{\frac{1}{2}} \to \left(\frac{\sigma\,(cos\theta_0 + cos\theta_1)}{\rho g \alpha}\right)^{\frac{1}{2}}. \quad \textbf{Eq. 17}$$

Consequently, the time evolution of the height of capillary rise of the fluid could be obtained as a function of the distance between the mesh plate and solid plates. Referring to the previous experiments, a rising height profile was obtained, as shown in Figure 29.

The line indicates the distribution of the liquid in the narrow gap between the stainless steel and mesh plates. Subsequently, the time evolutions of the height of capillary rise at different gap distances between the stainless steel plate and the mesh (or wick structure of the heat pipe) could be obtained by extracting data points along the y-axis (see arrow in Figure 29). Figure 29 shows the results of the data acquisition. Data sets of the height of capillary rise against time at different gap distances were set by dividing the data with scaling factors calculated from the properties of ethanol.

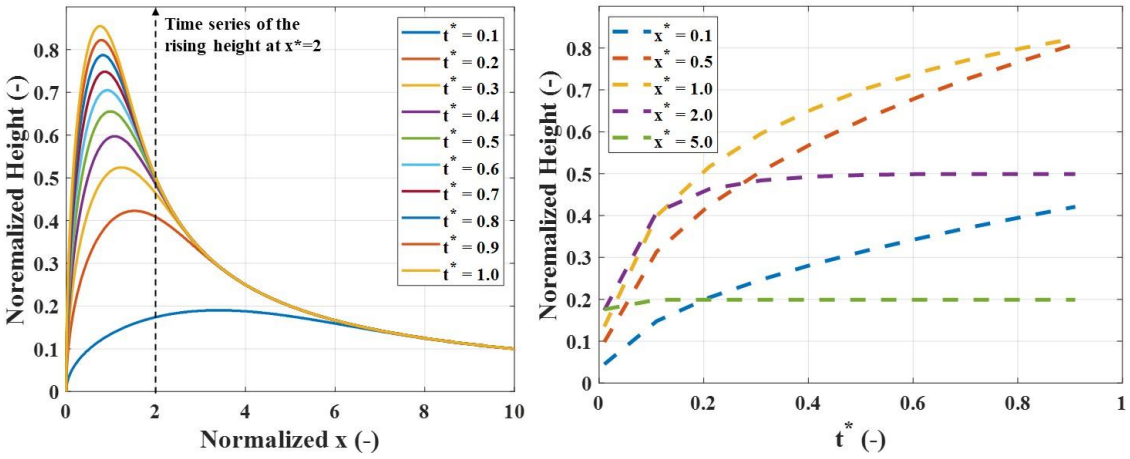

Figure 29. Rising height between mesh and solid plate making varying gap distance, calculated using the liquid properties of ethanol (left) and extracted information of the rising height evolution with different gap distances (right).

The last step for the analysis is to solve Eq. 2 using the rising height and time values. The height values were converted to mass by multiplying gap distance, unit distance (0.1 mm), and density of the ethanol. Similar to the previous discussion, the iteration method was adopted to solve the non-linear, transcendental equation having two unknowns. Figure 30 shows the results. The experimental data from Figure 25 are plotted in red and the results of this study, calculated from the analytical solution suggested by Higuera et al. (Higuera et al., 2008), are plotted in blue. The experimental result for the bare mesh with no solid plate is plotted as the dashed line. The analytical

calculation did not include factors such as shear stress at the surface, and extra capillary pressure caused by mesh, which could cause data offset. However, the value of the interest in this study was the peak point where the largest K/r_{eff} could be obtained. From this viewpoint, we noticed that both the experimental data and analytical calculation results demonstrate similar peak points. The experimental data has a peak at 1.20 mm of gap distance, whereas the analytical calculation has one at 1.26 mm of gap distance. The existence of the peak (or an optimal point) of the K/r_{eff} could be explained by trade-off of the gap effect. When the smallest gap distance was introduced, the capillary pressure from the gap was maximized. Moreover, the pressure drop caused by the shear stress of the channel decreased as the diameter of the channel, or the gap distance in this study, increased.

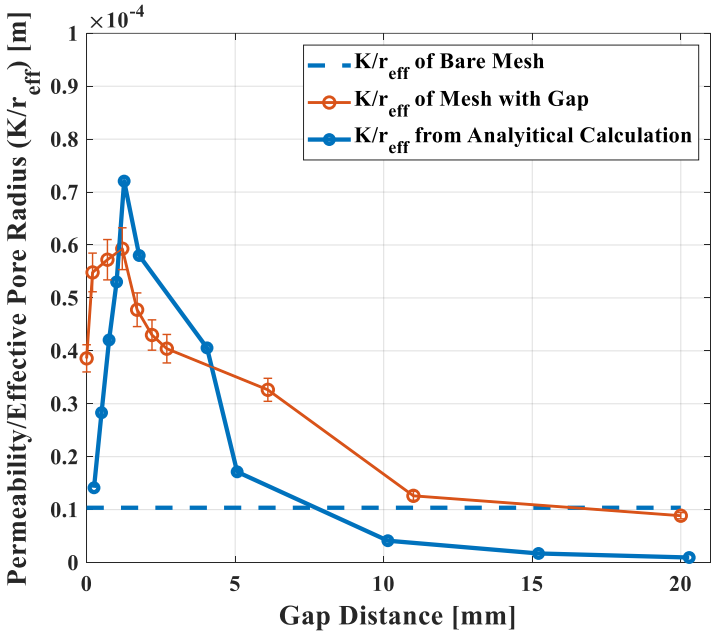

Figure 30. Result of K/r_{eff} at different gap distances obtained from the experiment and from the analytical calculation.

The results of the optimal gap distance presented in this study could be useful for designing a heat pipe with an annular-type wick structure and using ethanol as a working fluid. Particularly, when the operating range of the heat pipe is known and its operation is

limited by a capillary limitation, a gap distance of approximately 1.2 mm can be selected, because the capillary limitation is known to be highly affected by the geometry and characteristics of the wick structure.

3.3. Heat Pipe Performance Experimental Result

3.3.1. Performance Experimental Result

Figure 31 presents the results of the experiment. Points marked as circles indicate when the heat pipe was operating in normal conditions. The boundary conditions where heat pipe encountered capillary limitation, determined by a rapid increase in surface temperature, are marked with a cross. With some boundary conditions, temperature fluctuations occurred for several minutes with no rapid temperature increase. These points, marked with triangles, are considered a boundary between the normal operation heat pipe failure.

The capillary limitation of the bare mesh was calculated from Eq. 6 using the K/r_{eff} ratio determined by the mesh characterization experiment results. The calculated value of the bare mesh is used as a standard value to calculate the capillary limitation of the heat pipe with an annular type wick structure. The main idea here is that the capillary limitation calculated from Eq. 6 is assumed to present the limitation of the heat pipe without a gap between the wall and mesh. Based on this, a multiplying factor (G) is introduced. The factor was calculated simply by dividing K/r_{eff} values of the wick structure with different gap sizes which

are presented in Figure 25 by a K/r_{eff} value of the wick with 0 mm gap distance. The results are shown in Table 3. By introducing the multiplying factor, the capillary limitation

of the heat pipe with an annular type wick structure can be calculated using the following equation.

$$Q_{capillary.gap} = G \cdot Q_{capillary} = G \frac{2\sigma}{r_{eff}} \frac{KA_{wick} h_{lv} \rho_l}{\mu_l L_{eff}} \qquad \textbf{Eq. 18}$$

Based on the gap size of 0.95 mm, a value was 1.51 was used for the G value of the current heat pipe. As shown in Figure 31, this prediction is in strong agreement with the experimental results. As expected, heat pipe normally operates above the predicted power by traditional correlation without the consideration of the gap effect. Based on the result, the correlation suggested in this study can be used to predict the capillary limitation of the heat pipe with annular wick structure instead of the one suggested for the heat pipe without any gap between the wick structure and the wall.

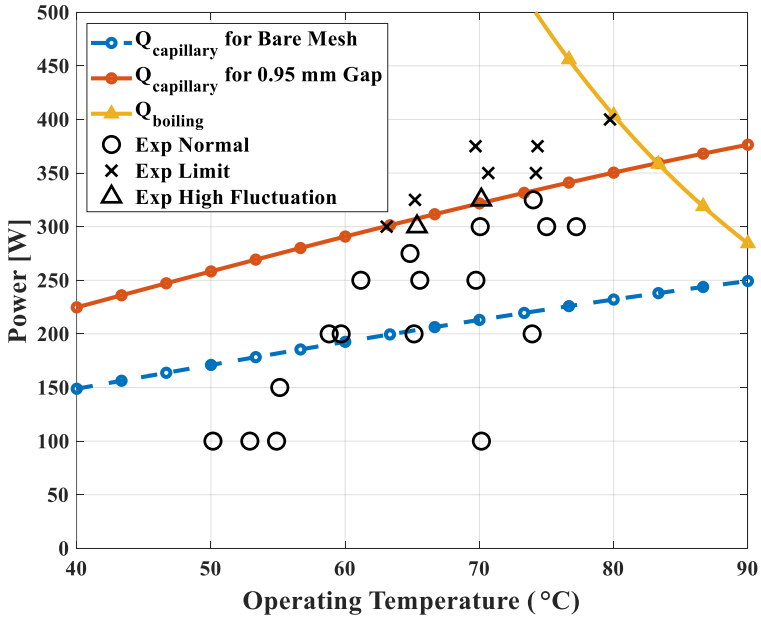

Figure 31. The result of heat pipe operating limitation experiment.

Table 3. Gap multiplying factor for capillary limitation.

Gap Distance [mm]	G [-]
0	1.00
0.2	1.42
0.7	1.48
1.2	1.54
1.7	1.24
2.2	1.11
2.7	1.05

3.3.2. Temperature Distribution Measurement Result

The results of the temperature distribution measurement at the start-up state of the heat pipe using fiber optic sensors are displayed in Figure 32. Using a 30W heater and measuring for 60 minutes. Although the actual result is a video, the video is screen captured at 15-minute intervals and displayed as a figure in this paper. Since the thermal couple sensor also recorded temperature, it is included in the graph. As a consequence, it was verified that the thermal couple sensor's temperature corresponded with the fiber optic sensor's temperature measurement value at the same position. The heat pipe was heated from the evaporator section where the heater was located, confirming that the evaporator's temperature was gradually propagated to the adiabatic section. Since the continual cooling of the condenser part, the temperature propagated up to but not beyond that point. Except for the sensor positioned on the heat pipe's external surface, the sensors located on the gap, inner mesh surface, and core within the heat pipe all displayed almost identical temperature values with no appreciable temperature difference. The outside sensor was immediately heated by the heater, resulting in high temperature measurement in the evaporator part, and it was also observed that the temperature decreased first owing to the coolant's direct action even in the condenser portion. Additionally, another fiber optic sensor was placed directly above the heater to allow for the measurement of the heater's temperature value independently.

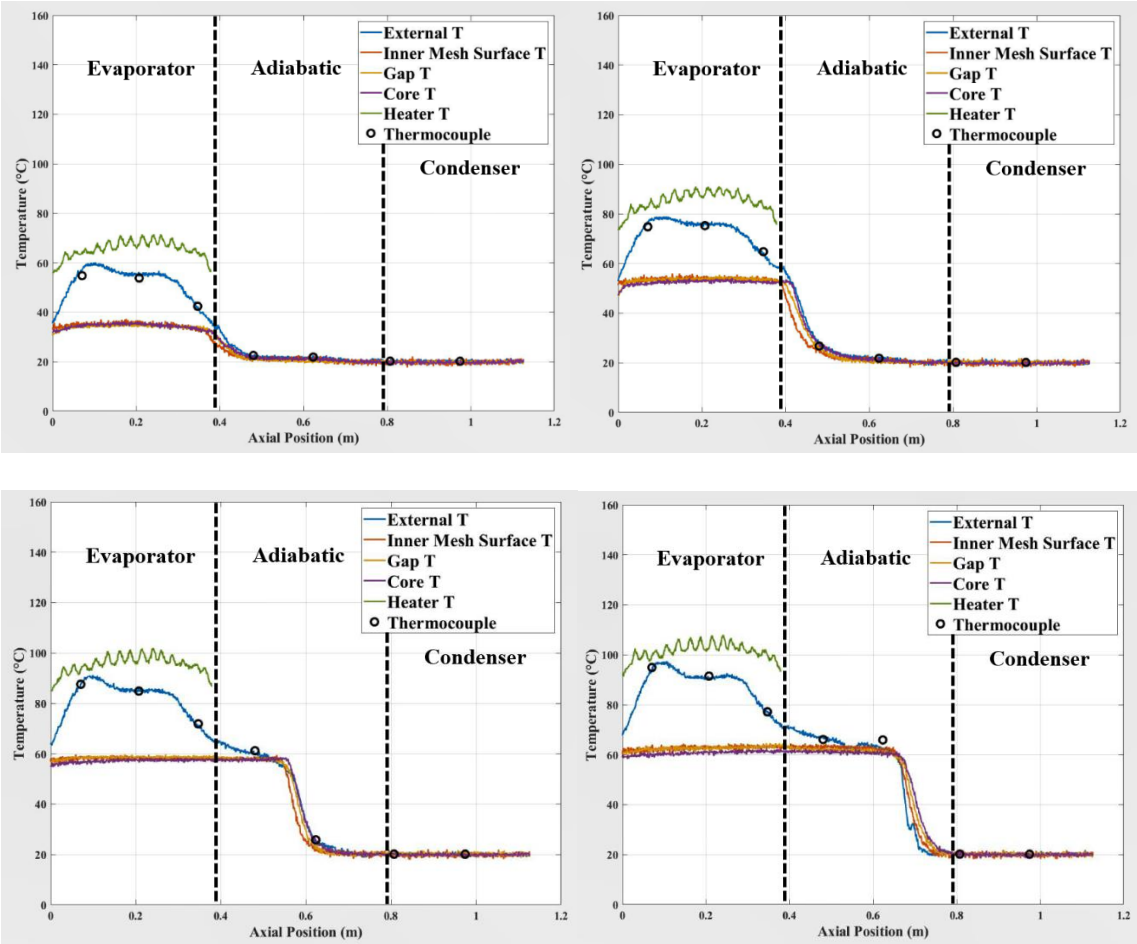

Figure 32. Temporal evolution of temperature distribution during a slow start up case (30 W heating power, during 60 mins)

The outcome of measuring the temperature change while the heat pipe experiment device is started up by quickly increasing the heater's temperature at the start is shown in Figure 33. The heater's wattage was instantly upped to 70W and the temperature was recorded for 60 minutes. As a consequence, a significant temperature increase occurred in a particular portion of the evaporator. As time passed, the temperature steadily grew, and it was discovered that the heat pipe had surpassed its operating limit. Since the goal of this

research is to confirm observed findings, the cause for this limitation was not studied in this experimental work.

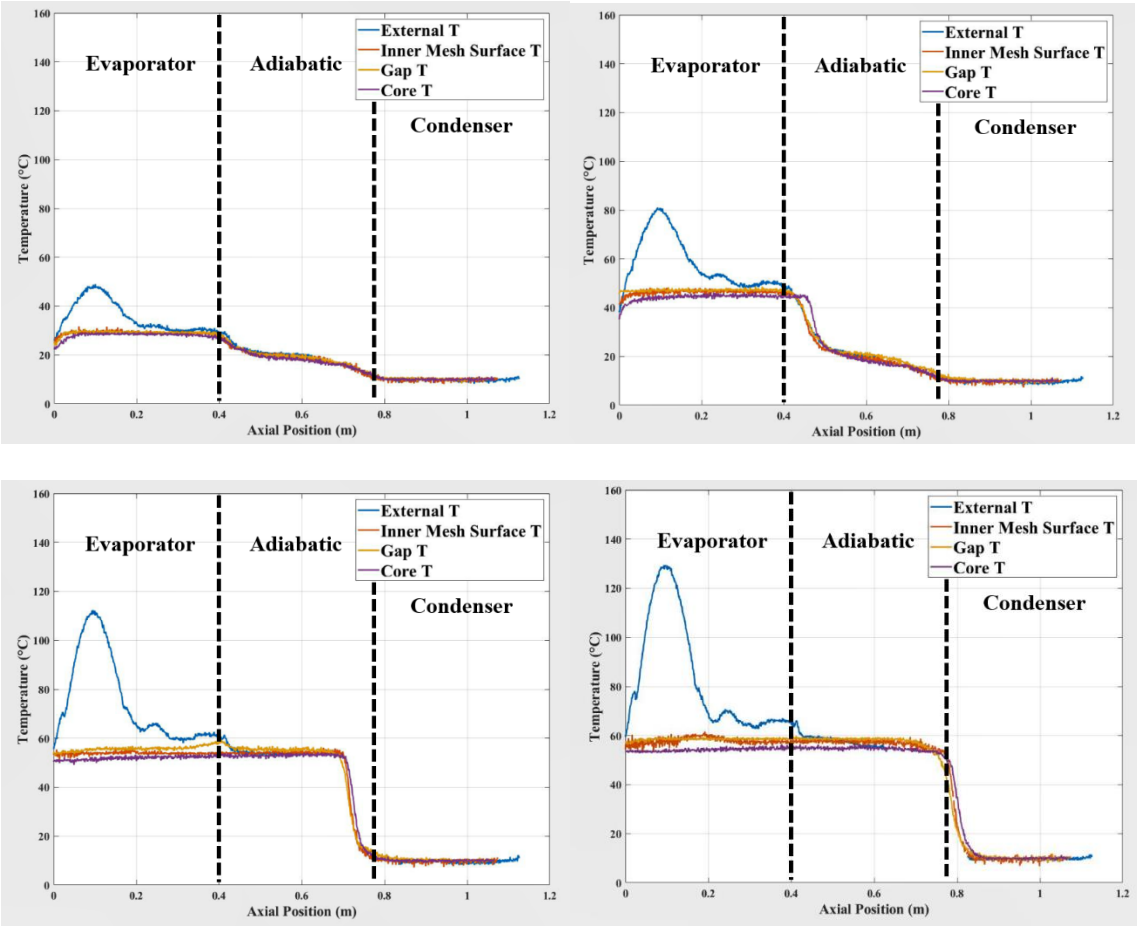

Figure 33. Temporal evolution of temperature distribution during a rapid start up case (75 W heating power, during 60 mins)

The following experiment established how the temperature distribution changed when the condenser section of the heat pipe was cooled to various degrees and then started. The temperature change was measured for 60 minutes during the initial start-up time while heating the heater with 25W power. Experiments were conducted using cooling temperatures of 10 degrees, 20 degrees, and 30 degrees. Each experimental outcome data video was captured at 15-minute intervals and is shown in Figure 34. The heat pipe cooled

to 30 degrees exhibited characteristically sluggish temperature propagation toward the adiabatic and maintained a high overall heat pipe operating temperature. On the other hand, the heat pipe chilled to 10 or 20°C propagated temperature rapidly and kept the working temperature below 40°C.

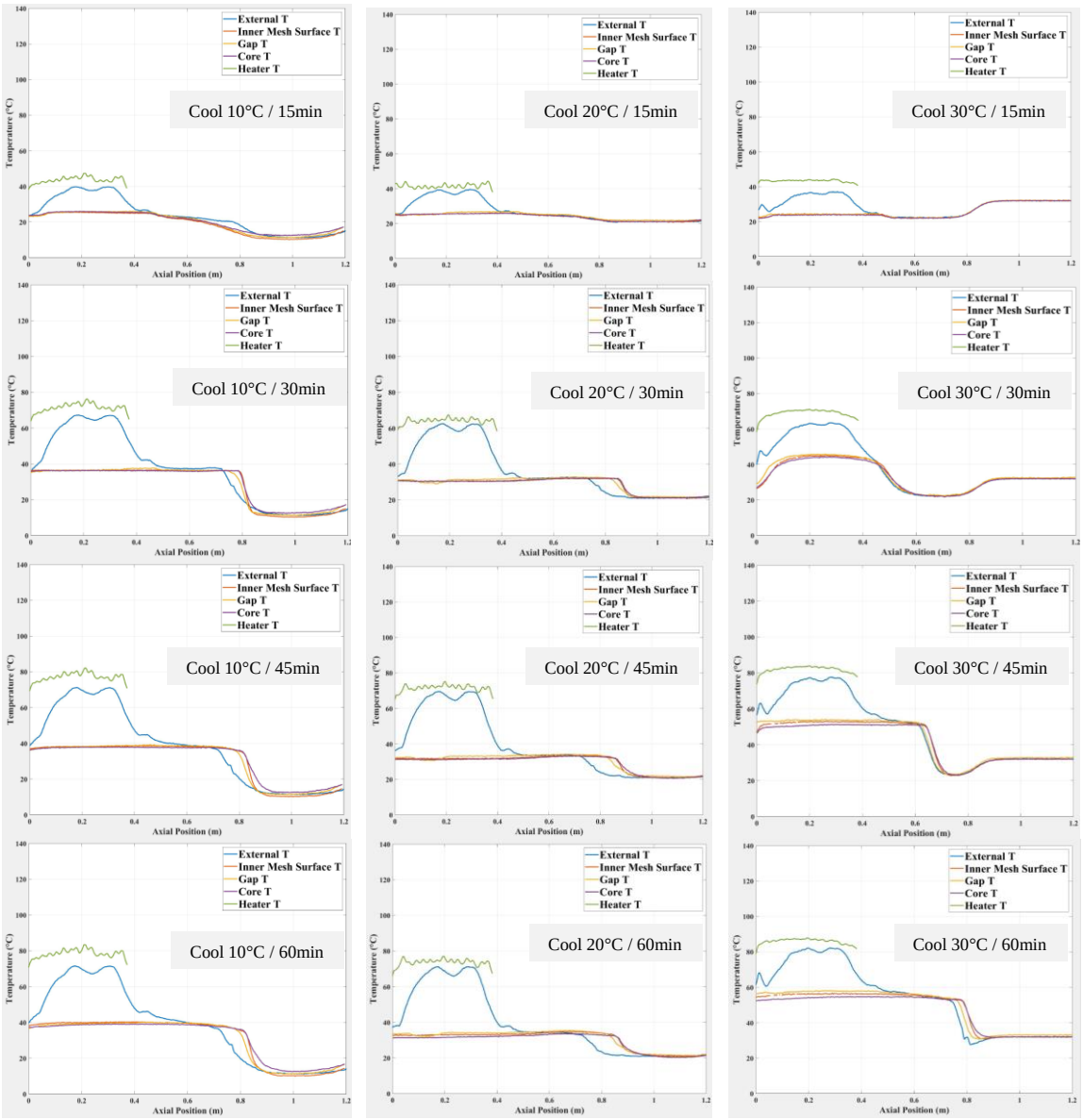

Figure 34. Temporal evolution of temperature distribution according to the change of cooling temperature (left: 10°C, middle: 20°C, right: 30°C)

The purpose of this paper was to visually observe how the heat pipe's temperature distribution varies over time and with different power and cooling temperatures during the heat pipe's startup phase. It was established that using a fiber optic sensor enabled reasonably precise and comprehensive temperature measurement and recording of the whole heat pipe, and meaningful experimental results were achieved and validated. Additional research and experimentation will be required in the future to conduct a detailed analysis and interpretation of the heat pipe's temperature distribution.

3.4. Heat Pipe Visualization Experimental Result

3.4.1. Boiling Pattern Inside Heat Pipe

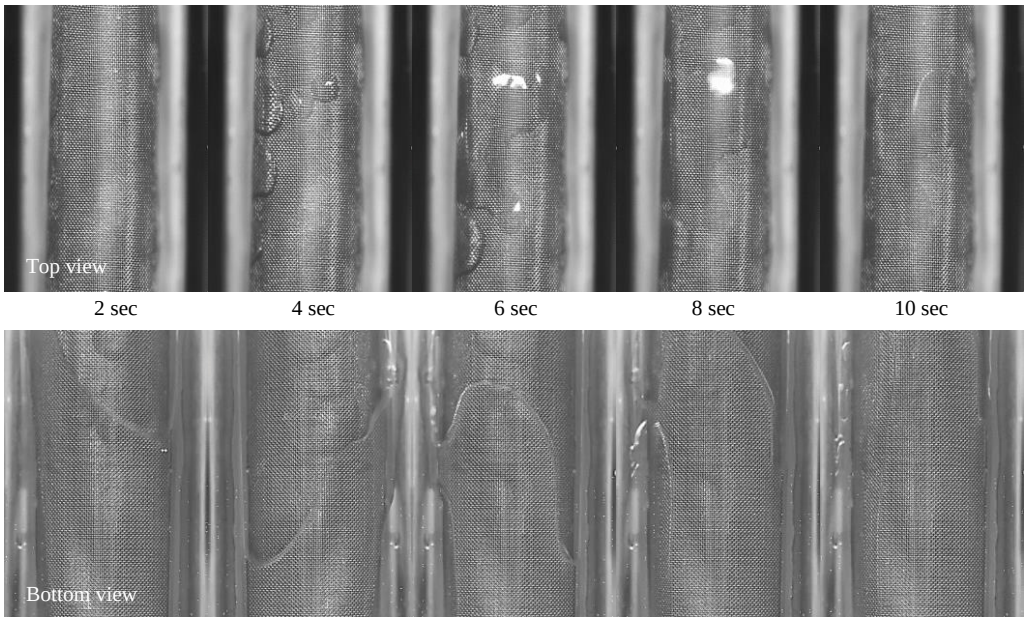

Figure 35. Top & Bottom view of the half wick heat pipe

Figure 35 depicts the two-second interval captured images from the video that was recorded when the boiling happened in the half-round circle annular wick heat pipe. As seen in Figure 18, the upper photos are top views (inside the wick) while the lower photos are bottom views (outside of the wick). When boiling occurs, the liquid fluctuates once,

and as the liquid is pushed into the inside of the wick, several water droplets are generated and then disappeared. The frequency of this type of boiling varies depending on the heating power of an evaporator. Figure 36 demonstrates the frequency of boiling that happens when the evaporator is powered by 100W, 200W, or 300W. As seen in the figure, boiling happens more frequently as the heater's power increases.

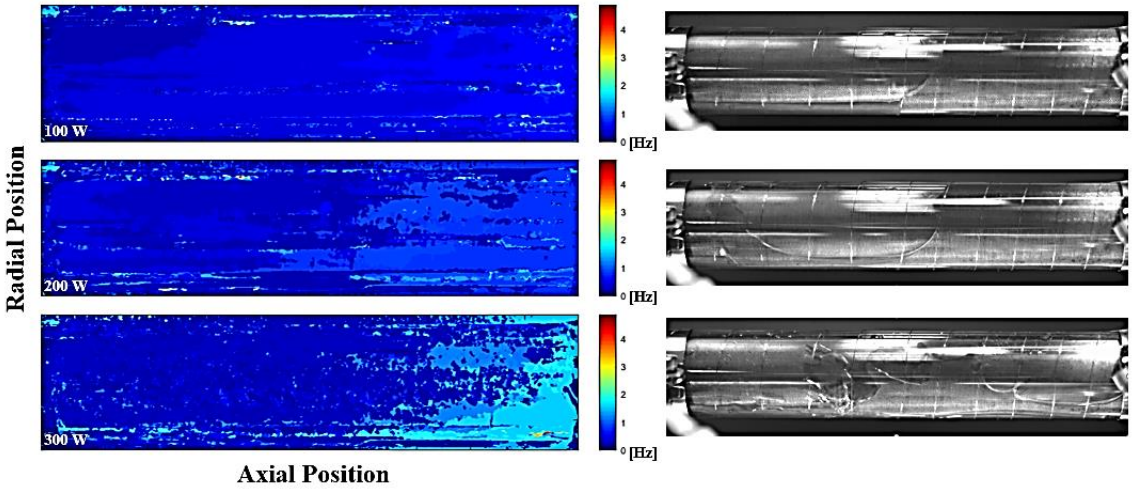

Figure 36. Boiling Frequency Analysis of the Evaporator Section

3.4.2. Heat Pipe Visualization with Inclination Angle

Figure 37, Figure 38, and Figure 39 show a comparison of how different boiling phenomena occur in a heat pipe evaporator depending on the inclination. A high-speed camera was used to record the upper side of the heat pipe's evaporator section. Images were captured at 1-second intervals from a 10-second video. As shown in Figure 21, since the condenser side of the heat pipe is raised to create a slope, the working fluid collects in the evaporator section as the slope increases. As a result, as the heat pipe's inclination increases, the boiling is compressed and occurs more intensely, and also it occurs greatly from bottom to top.

Figure 37. Heat Pipe Visualization Results - Inclination Effect (0-drgree, 100W)

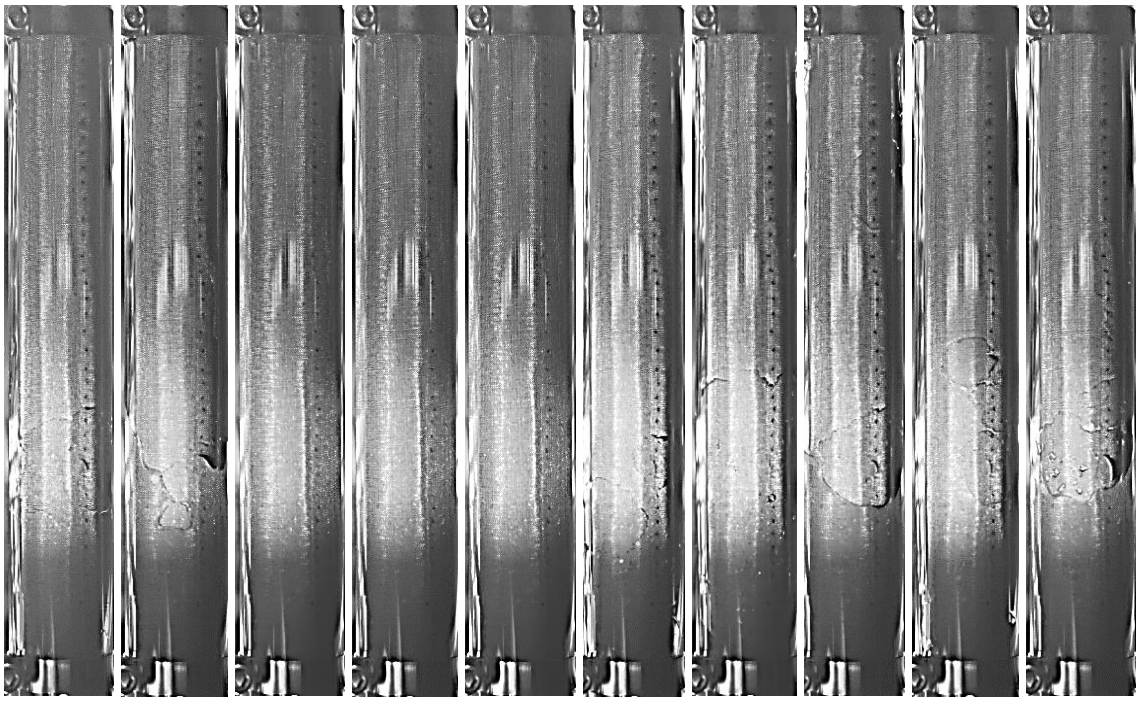

Figure 38. Heat Pipe Visualization Results - Inclination Effect (45-drgree, 200W)

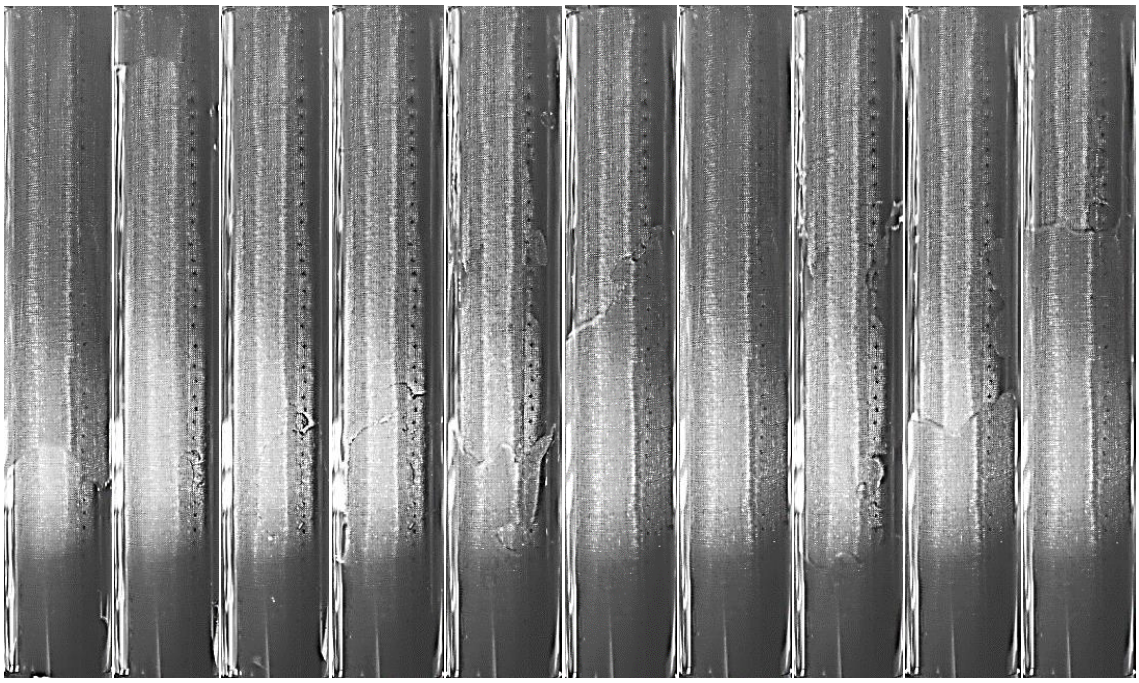

Figure 39. Heat Pipe Visualization Results - Inclination Effect (90-drgree, 200W)

The difference due to the inclination was also shown when the heat pipe was started up. Figure 40, and Figure 41 show the results of observation through fiber optic sensors installed on the top, side, and bottom surfaces of the heat pipe. In a horizontal heat pipe, it can be seen that the temperature of the top side rises rapidly during start-up because the fluid is only existed on the bottom due to gravity. However, when it is inclined at 45 degrees, the temperature difference between the top and bottom sides of the evaporator section is not large, and the overall evaporator's temperature becomes more stable, as the fluid accumulates throughout the evaporator section by gravity.

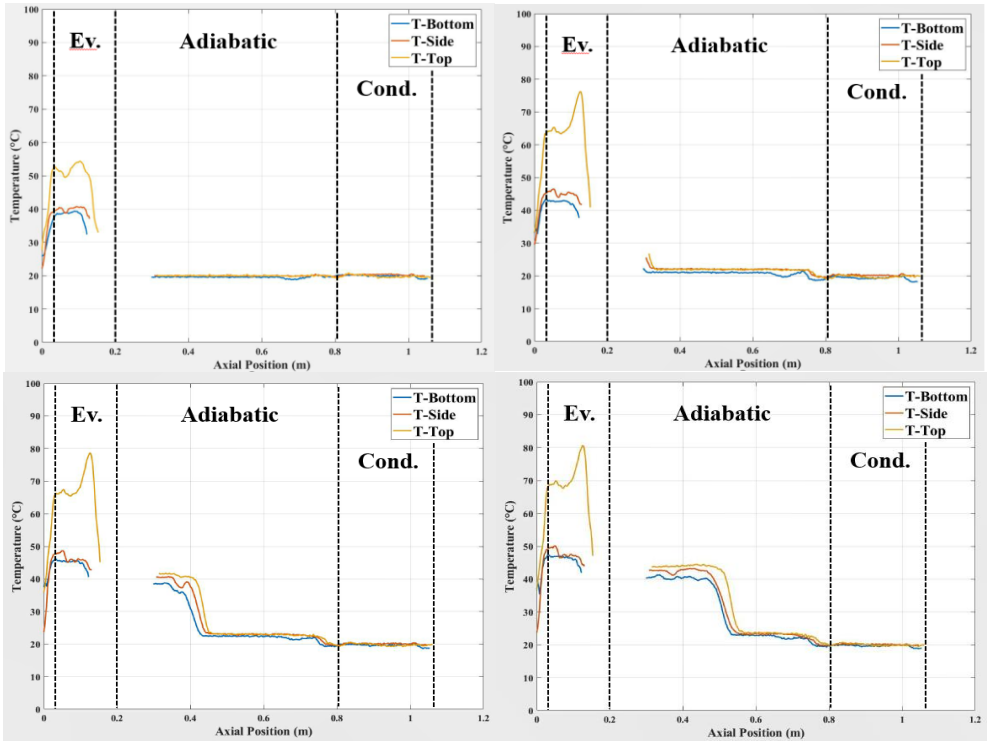

Figure 40. Temporal evolution of temperature distribution (0°, 25W startup)

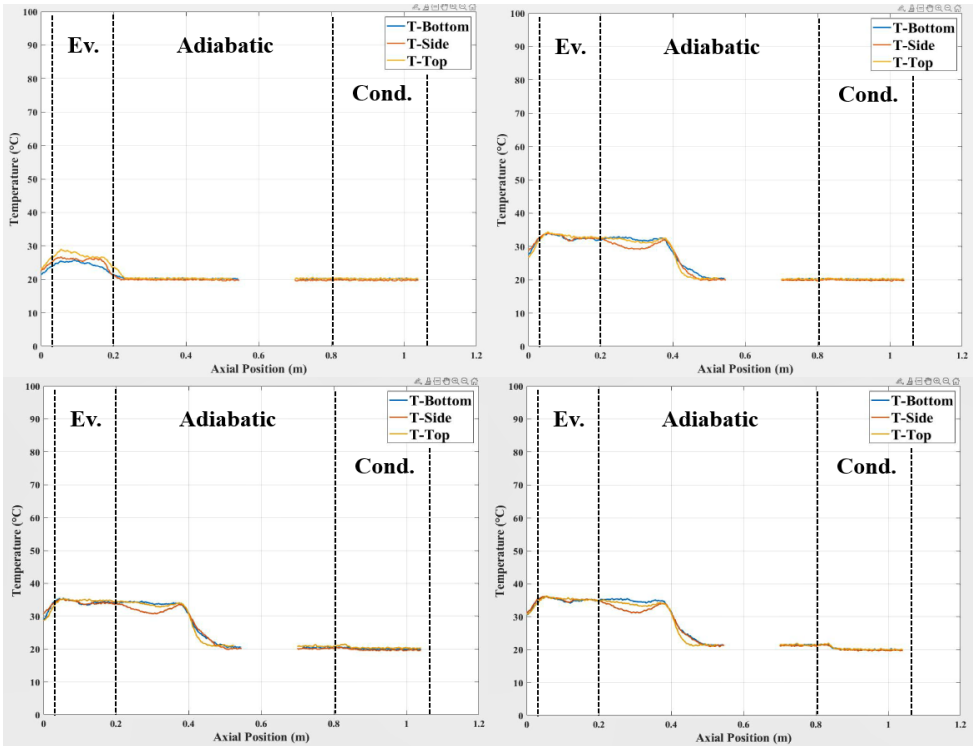

Figure 41. Temporal evolution of temperature distribution (45°, 25W startup)

Following that, with the heat pipe inclination set to 45 degrees, various power was provided to the heating (evaporator) section in order to visually inspect the inside of the heat pipe. As a result of recording and comparing the power of 100W, 200W, and 500W respectively, at 200W, boiling happens more frequently than at 100W, and at 500W, not only the frequency increase but also it can be confirmed that the boiling occurs larger and stronger.

3.4.3. Visualization of Operating limitation

When the heat pipe reached its operational limit, its temperature was monitored by installing an infrared camera beneath the heat pipe's evaporator, as described in Figure 20. The temporal variation of the evaporator has been recorded using an infrared camera. In Figure 42, the images on the left were captured from an infrared camera video of a horizontal heat pipe approaching its operating limit. The images on the right in Figure 42 were captured from a video of a 45° inclined heat pipe. As the working fluid in the heat pipe dries out, the pipe reaches its operating limit. When the heat pipe was horizontal, the liquid on both sides dried first, rapidly increasing the side temperature, and then the remaining liquid at the bottom dried, rapidly raising the bottom temperature. In the case of the 45-degree inclined heat pipe, on the other hand, the evaporator section was completely full of working fluid. As a result, the fluid dried completely immediately after being pushed out by the bubble created by the intense boiling, resulting in a rapid temperature increase.

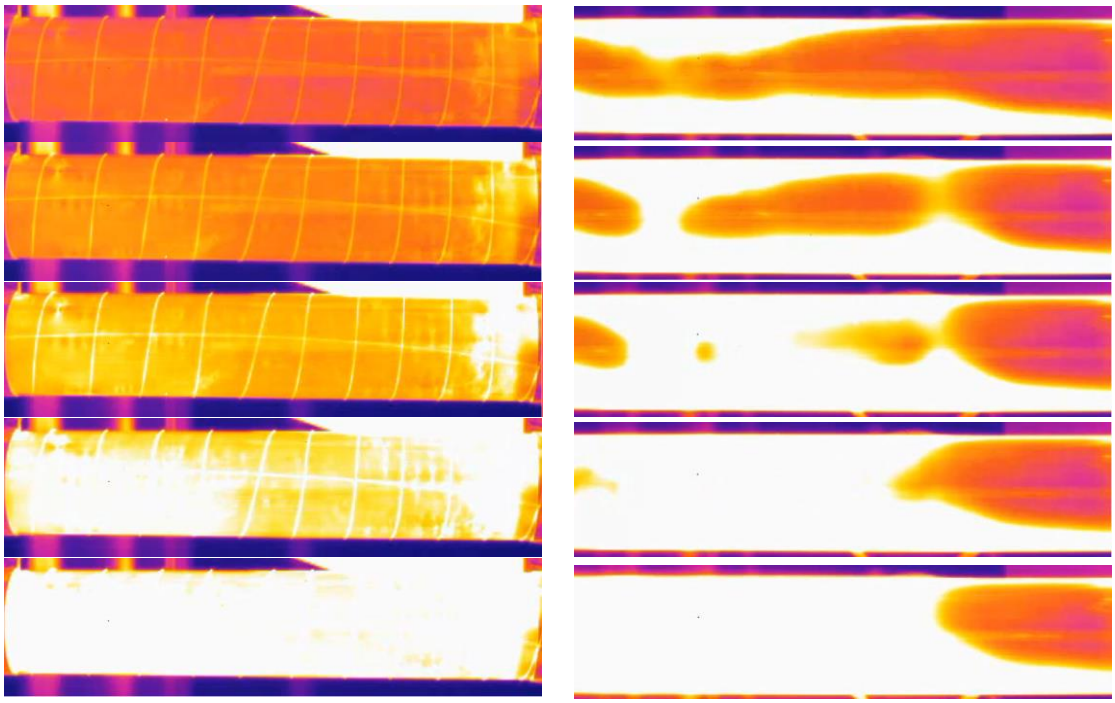

Figure 42. IR camera recording video image change when the heat pipe's operating limit is reached / 45° inclination (left) and 0° inclination (right)

The same phenomenon was confirmed by the temperature change data obtained with the fiber optic sensor that was installed as shown in Figure 19. When the horizontal heat pipe reaches its operating limit, it can be seen that the temperature at the bottom rises slightly later than the temperature at the top or side, as shown in Figure 43.

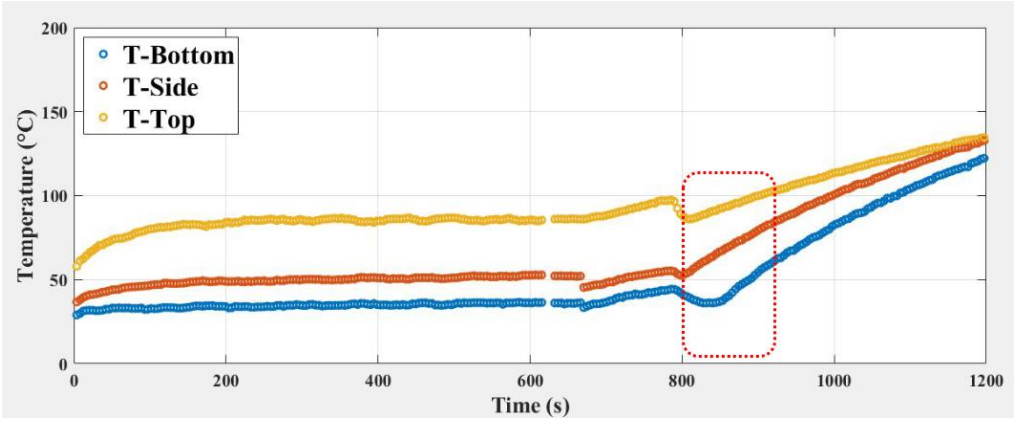

Figure 43. FOS temperature measurement result, Horizontal (0°), 100W (limit)

4. CONCLUSIONS[*] [**]

In this study, an experimental investigation was conducted on the hydraulic characteristics of annular type wick structures for heat pipes. An experimental facility was developed to measure porosity, permeability, and effective pore radius of wick structures in vacuum condition. Also, a heat pipe with an annular type wick structure was built and its capillary limitation was determined.

An experimental investigation was conducted on the contact angle of fluid in an annular wick-type heat pipe. Experiments were performed to measure the capillary rise between a solid plate and mesh wick plate at varying gap widths. Furthermore, a new model for calculating the height of capillary rise was suggested using the contact angle data of porous media. An additional experiment was performed to investigate the effect of curvature on the height of capillary rise.

Through the experimental investigation, the following results were found:

1. Nine different types of multi-layered (6 layers in total) composite screen meshes were characterized. Based on the measurement results, a wick structure composed of one layer of a 100×100 mesh, three layers of a 400×400 mesh, and two layers of a 60×60 mesh is determined to have the best performance.

---

[*] Reprinted with permission from "An experimental investigation on the characteristics of heat pipes with annular type composite wick structure" by Joseph Seo, Daegeun Kim, Hansol Kim, and Yassin Hassan, 2022, Nuclear Engineering and Design, vol. 390, 111701, copyright 2022 by Elsevier B.V. All rights reserved.

[**] Reprinted with permission from "Design Optimization of Gap Distance for the Capillary Limitation of a Heat Pipe with Annular-Type Wick Structure" by Joseph Seo, Daegeun Kim, Hansol Kim, and Yassin Hassan, 2022, Physics of Fluids, vol. 34, 067116, copyright 2022 Author(s). Published under an exclusive license by AIP Publishing.

2. The gap effect on the hydraulic characteristics of annular type wick structures is investigated. The measured permeability and effective pore radius of a wick with different gap distances showed that there is an optimal point in gap size which was found to be 1.2 mm.
3. A further exploration of the gap effect on the performance of the heat pipe was conducted. The time evolution of the height of capillary rise at different gap distances was analytically obtained. Additionally, the permeability and effective pore radius values were calculated and compared. Results revealed that the highest K/r_{eff} could be achieved in the heat pipe when the gap distance is 1.27 mm. The results showed good agreement with the optimal gap distance of the heat pipe suggested in a previous experimental study.
4. The effect of the gap on the performance of the heat pipe is tested using a heat pipe with an annular type wick structure. A multiplying factor to account for the enhanced performance of the wick provided by the gap is suggested. The calculated result showed good agreement with the experimental results.
5. The results of visually observing the inside heat pipe are useful for understanding the internal flow of the heat pipe and provided a revealing insight for further research.

Phenomena occurring inside heat pipes are highly complicated and have not yet been fully understood. Even though there are many models suggested by previous studies, models for heat pipes with annular type wick structures are limited to non-existent. This work provides insights into optimized design parameters and improved modeling

methods, essential for the construction of systems utilizing annular heat pipes. This study also lays the groundwork for additional works with similar approaches and extended experiments to provide a further understanding of phenomena occurring within annular, composite mesh wick heat pipes, as well as data for the validation of new models.

REFERENCES

Bullard, J. W., & Garboczi, E. J. (2009). Capillary rise between planar surfaces. *Physical Review E - Statistical, Nonlinear, and Soft Matter Physics*, *79*(1). https://doi.org/10.1103/PhysRevE.79.011604

Bushman, A., D.M. Carpenter, T.S. Ellis, S.P. Gallagher, M. D., Hershcovitch, M.C. Hine, E.D. Johnson, S.C. Kane, M. R. P., & A.H. Roach, S. Shaikh, M.P. Short, M. A. S. (2004). *The Martian Surface Reactor : An Advanced Nuclear Power Station for Manned Extraterrestrial Exploration*. *December*.

C. K. Batchelor and G. Batchelor. (2000). An Introduction to Fluid Dynamics. In *Cambridge university press* (Vol. 12, Issue 4). Cambridge university press. https://doi.org/10.1063/1.3060769

El-Genk, M. S. (2004). *Performance Analysis of Potassium Heat Pipes Radiator for HP-STMCs Space Reactor Power System*. 793–805. https://doi.org/10.1063/1.1649644

Faghri, A. (1995). *Heat Pipe Science And Technology*. Taylor & Francis.

Gaugler, R. S. (1944). *US Patent 2350348*.

Gotoh, M., & Hill, K. D. (1992). Temperature stability and reproducibility of pressure-controlled sodium-filled heat pipe furnaces. *Temperature, Its Measurement and Control in Science and Industry*, *6*(Part 2), 955–959.

Grover, G. M., Cotter, T. P., & Erickson, G. F. (1964). Structures of Very High Thermal Conductance. *Journal of Applied Physics*, *35*(6), 1990–1991. https://doi.org/10.1063/1.1713792

Hansel, J. E., Berry, R. A., Andrs, D., Kunick, M. S., & Martineau, R. C. (2021). Sockeye: A One-Dimensional, Two-Phase, Compressible Flow Heat Pipe Application. *Nuclear Technology*, *207*(7), 1096–1117. https://doi.org/10.1080/00295450.2020.1861879

Higuera, F. J., Medina, A., & Liñán, A. (2008). Capillary rise of a liquid between two vertical plates making a small angle. *Physics of Fluids*, *20*(10). https://doi.org/10.1063/1.3000425

Holley, B., & Faghri, A. (2006). Permeability and effective pore radius measurements

for heat pipe and fuel cell applications. *Applied Thermal Engineering*, *26*(4), 448–462. https://doi.org/10.1016/j.applthermaleng.2005.05.023

Jeong, Y. S., Kim, K. M., Kim, I. G., & Bang, I. C. (2015). Hybrid heat pipe based passive in-core cooling system for advanced nuclear power plant. *Applied Thermal Engineering*, *90*, 609–618. https://doi.org/10.1016/j.applthermaleng.2015.07.045

Khrustalev, D., & Faghri, A. (1994). Thermal analysis of a micro heat pipe. *Journal of Heat Transfer*, *116*(1), 189–198. https://doi.org/10.1115/1.2910855

Levinsky, A., Wyk, J. J., Arafat, Y., & S., M. C. (2018). Westinghouse eVinci Reactor for Off-Grid Markets. *Transactions of the American Nuclear Society*.

Manoj, R., Kumar, M. C., Narasimha Rao, R., Rama Narasimha, K., & Suresh, P. V. S. (2013). Performance Evaluation of Sodium Heat Pipe Through Parameteric Studies. *Frontiers in Heat Pipes*, *3*(4). https://doi.org/10.5098/fhp.v3.4.3003

Mathioulakis, E., & Belessiotis, V. (2002). A new heat-pipe type solar domestic hot water system. *Solar Energy*, *72*(1), 13–20. https://doi.org/10.1016/S0038-092X(01)00088-3

Mcclure, P. R., Poston, D. I., Dasari, V. R., & Reid, R. S. (2015). Design of megawatt power level heat pipe reactors. *Report of Los Alamos National Laboratory, USA*.

Mochizuki, M., Singh, R., Nguyen, T., & Nguyen, T. (2014). Heat pipe based passive emergency core cooling system for safe shutdown of nuclear power reactor. *Applied Thermal Engineering*, *73*(1), 699–706. https://doi.org/https://doi.org/10.1016/j.applthermaleng.2014.07.004

Mohamed S. El-Genk and Jean-Michel P.Tournier. (2004). “SAIRS” — Scalable Amtec Integrated Reactor space power System. *Progress in Nuclear Energy*, *45*(1), 25~69.

Mwaba, M. G., Huang, X., & Gu, J. (2006). Influence of wick characteristics on heat pipe performance. *International Journal of Energy Research*, *30*(7), 489–499. https://doi.org/10.1002/er.1164

Nguyen, A. V., Nalaskowski, J., & Miller, J. D. (2003). The dynamic nature of contact angles as measured by atomic force microscopy. *Journal of Colloid and Interface Science*, *262*(1), 303–306. https://doi.org/10.1016/S0021-9797(03)00123-1

Palac, D., Gibson, M., Mason, L., Houts, M., McClure, P., & Robinson, R. (2016). *Nuclear systems kilopower overview* (No. GRC-E-DAA-TN29740).

Paripatyadar, S. A., & Richardson, J. T. (1988). Cyclic performance of a sodium heat pipe, solar reformer. *Solar Energy, 41*(5), 475–485. https://doi.org/10.1016/0038-092X(88)90021-7

Pauluis, G., & Lang, S. B. (1976). Theoretical investigations of hydrogen, nitrogen, and oxygen homogenous and annular wick heat pipes. *Cryogenics*, *16*(7), 415–422. https://doi.org/10.1016/0011-2275(76)90055-2

Peterson, G. P. (1994). *An Introduction to Heat Pipes: Modeling, Testing, and Applications*. Wiley.

Piva, M. (2009). Capillary Rise in a Wedge. *The Physics Teacher*, *47*(8), 528–530. https://doi.org/10.1119/1.3246472

Pompe, T., & Herminghaus, S. (2000). Three-phase contact line energetics from nanoscale liquid surface topographies. *Physical Review Letters*, *85*(9), 1930–1933. https://doi.org/10.1103/PhysRevLett.85.1930

Poston, D. I. (2001, February). The heatpipe-operated Mars exploration reactor (HOMER). In *AIP Conference Proceedings* (Vol. 552, No. 1, pp. 797-804). American Institute of Physics.

Reid, R. S. (2003). *Sodium heat pipe module test for the SAFE-30 reactor prototype*. *87545*(505), 869–874. https://doi.org/10.1063/1.1358021

Richardson, J. T., Paripatyadar, S. A., & Shen, J. C. (1988). Dynamics of a sodium heat pipe reforming reactor. *AIChE Journal*, *34*(5), 743–752. https://doi.org/10.1002/aic.690340505

Rosenfeld, J. H., Ernst, D. M., Lindemuth, J. E., Sanzi, J. L., Geng, S. M., & Zuo, J. (2004, February). An overview of long duration sodium heat pipe tests. *In AIP Conference Proceedings* (Vol. 699, No. 1, pp. 140-147). American Institute of Physics.

Schuster, J. M., Schvezov, C. E., & Rosenberger, M. R. (2015). Influence of Experimental Variables on the Measure of Contact Angle in Metals Using the

Sessile Drop Method. *Procedia Materials Science*, *8*(2009), 742–751. https://doi.org/10.1016/j.mspro.2015.04.131

Seo, J., Kim, D., Kim, H., & Hassan, Y. A. (2022a). An experimental investigation on the characteristics of heat pipes with annular type composite wick structure. *Nuclear Engineering and Design*, *390*(February), 111701. https://doi.org/10.1016/j.nucengdes.2022.111701

Seo, J., Kim, D., Kim, H., & Hassan, Y. A. (2022b). Design Optimization of Gap Distance for the Capillary Limitation of a Heat Pipe with Annular-Type Wick Structure Design Optimization of Gap Distance for the Capillary Limitation of a Heat Pipe with Annular-Type Wick Structure. *Physics of Fluids*, *34*, 067116. https://doi.org/10.1063/5.0094561

Shukla, K. N. (2015). Heat pipe for aerospace applications—an overview. *Journal of Electronics Cooling and Thermal Control*, 5(01), 1.

Sundberg, M., Månsson, A., & Tågerud, S. (2007). Contact angle measurements by confocal microscopy for non-destructive microscale surface characterization. *Journal of Colloid and Interface Science*, *313*(2), 454–460. https://doi.org/10.1016/j.jcis.2007.04.067

Wilhelmy, L. (1863). Ueber die Abhängigkeit der Capillaritäts-Constanten des Alkohols von Substanz und Gestalt des benetzten festen Körpers. *Ann. Phys.*, *195*, 177–217. https://doi.org/10.1007/978-3-662-28327-1

Yan, B. H., Wang, C., & Li, L. G. (2020). The technology of micro heat pipe cooled reactor: A review. *Annals of Nuclear Energy*, *135*. https://doi.org/10.1016/j.anucene.2019.106948

Zhao, T., & Jiang, L. (2018). Contact angle measurement of natural materials. *Colloids and Surfaces B: Biointerfaces*, *161*, 324–330. https://doi.org/10.1016/j.colsurfb.2017.10.056